Sparse sampling of intermittent turbulence generated by breaking surface waves

Morteza Derakhti* and Jim Thomson

Applied Physics Laboratory, University of Washington, Seattle, WA.

James T. Kirby

Center for Applied Coastal Research, University of Delaware, Newark, DE.

**Corresponding author address:* Morteza Derakhti, derakhti@uw.edu

E-mail: derakhti@uw.edu

Generated using v4.3.2 of the AMS LaTeX template

Early Online Release: This preliminary version has been accepted for publication in *Journal of the Physical Oceanography*, may be fully cited, and has been assigned DOI 10.1175/JPO-D-19-0138.1. The final typeset copyedited article will replace the EOR at the above DOI when it is published.

ABSTRACT

Accepted for publication in *Journal of Physical Oceanography*. DOI 10.1175/JPO-D-19-0138.1.

We examine how Eulerian statistics of wave breaking and associated turbulence dissipation rates in a field of intermittent events compare with those obtained from sparse Lagrangian sampling by surface following drifters. We use a polydisperse two-fluid model with large-eddy simulation (LES) resolution and volume-of-fluid surface reconstruction (VOF) to simulate the generation and evolution of turbulence and bubbles beneath short-crested wave breaking events in deep water. Bubble contributions to dissipation and momentum transfer between the water and air phases are considered. Eulerian statistics are obtained from the numerical results which are available on a fixed grid. Next, we sample the LES/VOF model results with a large number of virtual surface-following drifters that are initially distributed in the numerical domain, regularly or irregularly, before each breaking event. Time-averaged Lagrangian statistics are obtained using the time-series sampled by the virtual drifters. We show that convergence of statistics occurs for signals that have minimum length of approximately 1000-3000 wave periods with randomly spaced observations in time and space relative to three-dimensional breaking events. We further show important effects of (i) extent of measurements over depth and (ii) obscuration of velocity measurements due to entrained bubbles, which are the two typical challenges in most of the available in situ observations of upper ocean wave breaking turbulence. An empirical correction factor is developed and applied to the previous observations of Thomson et al. (2016). Applying the new correction factor to the observations noticeably improves the inferred energy balance of wind input rates and turbulence dissipation rates. Finally, both our simulation results and the corrected observations suggested that the total wave breaking dissipation rates have a nearly linear relation with active whitecap coverage.

Accepted for publication in *Journal of Physical Oceanography*. DOI 10.1175/JPO-D-19-0138.1.

1. Introduction

Many previous studies have shown that turbulence dissipation rates in the ocean surface layer are elevated in the presence of breaking waves (e.g., Agrawal et al. 1992; Terray et al. 1996; Gemmrich and Farmer 2004; Gemmrich 2010; Thomson 2012; Sutherland and Melville 2015). This turbulence is important as an input of energy from the wind to the ocean (Gemmrich et al. 1994), a sink of energy for the surface waves (Melville 1996), and a driver of air-sea gas exchange (Zappa et al. 2007). The turbulence is complicated by two-phase flow, in which bubbles are active particles (e.g., Rapp and Melville 1990; Lamarre and Melville 1991; Derakhti and Kirby 2014a; Deike et al. 2017a). Another challenge is the intermittent nature of the forcing, with individual waves breaking as a result of random phase interference patterns and modulational instability (Babanin 2011).

Direct measurements of the turbulence beneath breaking surface waves are rare. Recent examples have employed a surface-following reference frame (e.g., Gemmrich 2010; Thomson 2012; Sutherland and Melville 2015; Zippel et al. 2018), which is a natural choice for the observations but a challenge to reconcile with the fixed (Eulerian) reference frames common in numerical models. Furthermore, the observations generally are sparse in space and time, such that it has been difficult to ensure robust statistics. Published observations of turbulence in the ocean near-surface layer generally find that 1) turbulence levels greatly exceed those predicted by law-of-the-wall shear scaling, and 2) this wave-enhanced layer is limited to a depth of approximately one significant wave height in a fixed reference frame (or 1 to 2 m in a wave-following reference frame) (Esters et al. 2018). As most of these observations use acoustic Doppler methods to obtain turbulent fluid velocities, the data in the most active portion of the breaking waves are often occluded

Accepted for publication in *Journal of Physical Oceanography*. DOI 10.1175/JPO-D-19-0138.1.

by bubbles. Thus, existing observations likely represent an incomplete average of the surface conditions, which lack the maxima occurring in space and time.

Numerical models and laboratory experiments have been essential in filling the gaps, *e.g.*, quantifying turbulence-bubble interaction in bubbly flows beneath breaking waves and providing a high-resolution spatio-temporal variation of turbulence dissipation rates during active breaking. The early studies of Rapp and Melville (1990) and Lamarre and Melville (1991) established time and length scales for the turbulence from two-dimensional focused wave packets, including the importance of bubbles in the setting of the total dissipation. More recently, Wang and Wijesekera (2018) conducted a large-scale laboratory experiment with three-dimensional (3-D), *i.e.*, short-crested, breaking crests in a modulated wave train. Their measurements showed that values of near-surface turbulence dissipation rates during an active breaking event is two to three orders of magnitude larger than those before and after the wave breaking. The recent numerical efforts of Derakhti and Kirby (2014a, 2016) and Deike et al. (2016, 2017a) resolve the breaking of individual waves and the associated turbulence and bubble dynamics. Derakhti and Kirby (2014a) results showed that high dissipation rates occurs preferentially in regions with high void fraction within bubble plumes. Furthermore, their simulation results predicted that bubble-induced dissipation accounts for approximately 50% of the total wave-breaking-induced turbulence dissipation regardless of breaker type and intensity. Here, bubble-induced dissipation refers to the enhancement of turbulence dissipation due to the subgrid-scale (SGS) turbulent motions generated by the dispersed bubbles (see Derakhti and Kirby 2014a, §4.3.1 for more details).

The present work is motivated by the study of Thomson et al. (2016), in which turbulence dissipation rates were estimated using Doppler velocity profiles within the upper meter of the wave-following surface. That study concluded that strong turbulence is isolated to a very thin layer (< 1 m), but that orbital motions advect the turbulence over vertical scales of at least one significant

Accepted for publication in *Journal of Physical Oceanography*. DOI 10.1175/JPO-D-19-0138.1.

wave height. The main focus of Thomson et al. (2016) was evaluating the energetic balance at the surface, with the conclusion that the observed energy dissipation rates were insufficient to balance the energy input rates using several different formulations.

Here, we revisit the topics of Thomson et al. (2016) by sampling a high-fidelity numerical model in the Lagrangian mode of the surface-following observations. We use a polydisperse two-fluid model (Derakhti and Kirby 2014a) with large-eddy simulation (LES) resolution and volume-of-fluid surface reconstruction (VOF) to simulate the generation and evolution of turbulence and bubbles beneath 3-D short-crested wave breaking events in deep water (§2). We first scale the model domain to match the observed whitecap coverage values, and we scale the model wave heights to match the wind-wave (*i.e.*, equilibrium) portion of the observed spectrum (*i.e.*, neglecting swell). We then determine the effects of sparse sampling and intermittent breaking, as well as the effects of data occlusion by bubbles and limitations in the vertical extent of the observed profiles (§3). In §4, we comment on the apparent discrepancy between the observed wind-input energy fluxes and total turbulence dissipation rates reported by Thomson et al. (2016). Examination of potential Lagrangian sampling bias related to a partially trapped drifter in convergence zones in the turbulence observations is left for future work.

2. Methods

In this section, we first present the model governing equations for continuity of mass and momentum of liquid and gas phases of a polydisperse two-fluid mixture, as described in Derakhti and Kirby (2014a). The model set-up including details of the incident wave conditions and the scaling of the model domain to match observations of whitecap coverage are then described. Finally, we explain our methodology to convert the model results to surface following virtual drifters.

Accepted for publication in *Journal of Physical Oceanography*. DOI 10.1175/JPO-D-19-0138.1.

Demonstrations of model convergence and performance, including detailed comparisons of free surface evolution, bubble void fraction, integral properties of the bubble plume, organized and turbulent velocity fields and total wave-breaking-induced energy dissipation, for various deep- and shallow-breaking waves may be found in (Derakhti and Kirby 2014a,b, 2016; Derakhti et al. 2018, 2019).

a. Mathematical formulations

The computations here are performed using the LES/VOF Navier-Stokes solver TRUCHAS (Francois et al. 2006) with extensions of a polydisperse bubble phase and various turbulence closures (Carrica et al. 1999; Ma et al. 2011; Derakhti and Kirby 2014a). Details of the mathematical formulations and numerical method may be found in Derakhti and Kirby (2014a, §2).

The filtered governing equations for continuity of mass and momentum of the liquid phase are given by (Derakhti and Kirby 2014a):

$$\frac{\partial \alpha\rho}{\partial t} + \frac{\partial \alpha\rho\tilde{u}_j}{\partial x_j} = 0, \tag{1}$$

$$\frac{\partial \alpha\rho\tilde{u}_i}{\partial t} + \frac{\partial \alpha\rho\tilde{u}_i\tilde{u}_j}{\partial x_j} = \frac{\partial \Pi_{ij}}{\partial x_j} + \alpha\rho g\delta_{3i} + \mathbf{M}^{gl}, \tag{2}$$

where $(i,j) = 1,2,3$; ρ is a constant liquid density; α and $\tilde{u}_i$ are the volume fraction and the filtered velocity in the i direction of the liquid phase respectively; δ_{ij} is the Kronecker delta function; g is the gravitational acceleration; and $\Pi_{ij} = \alpha(-\tilde{p}\delta_{ij} + \tilde{\sigma}_{ij} - \rho\tau_{ij})$ with $\tilde{p}$ the filtered pressure, which is identical in each phase due to the neglect of interfacial surface tension, $\tilde{\sigma}_{ij}$ viscous stress and τ_{ij} the SGS stress estimated using an eddy viscosity assumption and the Dynamic Smagorinsky model, which includes liquid/bubble interaction effects (for more details see Derakhti and Kirby 2014a, §2.4). Finally, $\mathbf{M}^{gl}$ are the momentum transfers between liquid and gas phases, including the filtered virtual mass, lift, and drag forces (Derakhti and Kirby 2014a).

Accepted for publication in *Journal of Physical Oceanography*. DOI 10.1175/JPO-D-19-0138.1.

Using the same filtering process as in the liquid phase, the equations for the bubble number density and continuity of momentum for each bubble size class with a diameter d_k^b, $k = 1, \cdots, N_G$, are then given by (Derakhti and Kirby 2014a):

$$\frac{\partial N_k^b}{\partial t} + \frac{\partial \tilde{u}_{k,j}^b N_k^b}{\partial x_j} = R_k^b, \tag{3}$$

$$0 = -\frac{\partial \alpha_k^b \tilde{p}}{\partial x_j}\delta_{ij} + \alpha_k^b \rho^b g_i + \mathbf{M}_k^{lg}, \tag{4}$$

where m_k^b, N_k^b, $\alpha_k^b = m_k^b N_k^b / \rho^b$, and $\tilde{u}_{k,j}^b$ are the mass, number density, volume fraction, and filtered velocity in the j direction of the kth bubble size class; ρ^b is the bubble density; and R_k^b includes the source due to air entrainment in the interfacial cells (Derakhti and Kirby 2014a, §2.3), intergroup mass transfer, and SGS diffusion terms. Finally, $\mathbf{M}_k^{lg}$ represents the total momentum transfer between liquid and the kth bubble size class, and satisfies $\mathbf{M}^{gl} + \sum_{k=1}^{N_G} \mathbf{M}_k^{lg} = 0$. In (4), we neglect the inertia and shear stress terms in the gas phase following Carrica et al. (1999) and Derakhti and Kirby (2014a).

b. Model set-up

Our numerical experiments are carried out in a virtual wave tank of unperturbed constant depth h, extending a length L_x in the x direction, and $\pm L_y/2$ in the transverse y direction. The vertical direction z in the fixed reference frame is positive upward and measured from the still water level. The virtual wave tank is sufficiently deep to avoid any depth-limited wave breaking, such that the experiments remain focused on whitecaps.

All simulations are performed with the model initialized with quiescent conditions. An incident wave packet is then generated at the model upstream boundary ($x = 0$). The input focused wave packet was composed of $N = 10$ sinusoidal components of steepness $a_n k_n, n = 1, \cdots, N$, where a_n and k_n are the amplitude and wave number of the nth frequency component. The steepness of

Accepted for publication in *Journal of Physical Oceanography*. DOI 10.1175/JPO-D-19-0138.1.

individual wave components is taken to be constant across the spectrum, or $a_1k_1 = a_ik_i = ... = a_Nk_N = S_g/N$ with $S_g = \sum_{n=1}^{N} a_nk_n$ taken to be a measure of the wave train global steepness. Based on linear theory, the free surface elevation for the 3-D short-crested focused packets (Wu and Nepf 2002; Derakhti et al. 2018; Kirby and Derakhti 2019) at the wavemaker is given by

$$\eta(0,y,t) = \sum_{n=1}^{N} a_n \cos[2\pi f_n(t-t_f) + \frac{k_n x_f}{\cos\theta(y)}], \tag{5}$$

where f_n is the frequency of the nth component, x_f and t_f are the predefined, linear theory estimates of location and time of the focal point respectively, and $\theta(y)$ is the angle of incidence of each wave component at various transverse locations with $\cos\theta(y) = x_f/\sqrt{x_f^2+y^2}$. The discrete frequencies f_n were uniformly spaced over the band $\Delta f = f_N - f_1$ with a central frequency defined by $f_c = (f_N + f_1)/2$. Increasing the global steepness S_g and/or decreasing $\Delta f/f_c$ increases the total wave energy loss due to the resulting breaking event(s) in the virtual tank. Finally, liquid velocities for each wave component are calculated using linear theory and then superimposed at the wavemaker.

We define the spectrally-weighted frequency of the wave field f_s as

$$f_s = \frac{\int fE(f)df}{\int E(f)df}, \tag{6}$$

where E [m^2s] is the power spectral density of the wave field. The characteristic wave length L_s and period T_s are then calculated based on f_s and using the linear dispersion relation (as in Tian et al. 2010; Derakhti and Kirby 2016). The reference x-location x^* is taken as the location at which the first forward-moving jet of considered breaking events in a numerical case hits the undisturbed free surface, and is normalized by L_s. Further, we define $y^* = y/L_s$ and $z^* = z/L_s$.

Each numerical case is defined by setting the geometry of the virtual tank and the input wave packet. Here, three representative cases are considered, with all relevant parameters summarized

Accepted for publication in *Journal of Physical Oceanography*. DOI 10.1175/JPO-D-19-0138.1.

in Table 1. In all cases, most of the wave components in the input packets are characterized as deep water waves.

Figure 1a shows the temporal variation of the normalized free surface elevations at the center of the tank and slightly upstream of the break point, $(x^*, y^*) = (-0.1, 0)$, for the case T1. The results indicate that the current wavemaker setup (Eq. 5) results in a repeatable sequence of waves in the incident packet with a period of $T_g = N/\Delta f$. In all cases, the observed main breaking events in the virtual tank occur approximately every T_g. As shown in Figure 1a,d,e, however, the incident waves and the x-location of the main breaking event within each T_g are not the same; this may be partially because of seiching in the virtual tank and reflections from the numerical boundaries.

We only consider the model results for $t > t_0$ for all the analyses presented in this paper, where $t_0 > 12T_g > 200s$ is a time after which the background turbulence levels reach a quasi-steady state. For each case, we define the main breaking event Em ($m = 1, 2, \ldots, N_E$) as the most energetic breaking event that occurs in $m - 1 < (t - t_0)/T_g < m$. The total number of considered main breaking events N_E for the cases T1, T2, and T3 are 9, 10, and 6 respectively. Thus considering an output sampling rate of f_{out}, the time series of all Eulerian variables predicted by the model have $N_E T_g f_{out}$ data points, where f_{out} was 20 Hz for T1 and T2, and 25 Hz for T3.

c. Matching the model and observed conditions

We need to choose a number of well-defined parameters to present both the wave breaking forcing and model results in a non-dimensional form, such that they can be appropriately scaled to field conditions. Here our goal is to have the wave spectrum E and the fractional area of breaking crests of the simulated cases as consistent as possible with those observed in the field. The latter is usually referred to as the active part of the whitecap coverage W of visible breaking crests, hereafter referred to as W_A, which is a space- and time-averaged quantity calculated over a given

Accepted for publication in *Journal of Physical Oceanography*. DOI 10.1175/JPO-D-19-0138.1.

domain. There is a growing body of literature documenting a direct relationship between W_A and the total wave breaking energy dissipation in the upper ocean (Callaghan et al. 2016, 2017; Callaghan 2018; Anguelova and Hwang 2016). We also need a characteristic breaking wave height to scale the vertical profiles of wave-breaking-related dynamical measures, such as the turbulence dissipation rates.

Figure 1b shows the normalized power spectral density $E^* = EH_{eq}^{-2} f_s$ at $(x^*, y^*) = (-0.1, 0)$ for all three simulated cases, the vertical dashed lines show the frequency range of wave components in the input packet for each case. Figure 1c shows examples of observed E^* for various values of whitecap coverage W and wind speed U_{10} in the vicinity of OWS-P at 50° N, 145° W provided by Schwendeman and Thomson (2015); Thomson et al. (2016). Here we define H_{eq} as a characteristic breaking wave height given by

$$H_{eq} = 4\sqrt{\int_{f_s}^{2f_s} E(f)df}. \tag{7}$$

The results demonstrate that both the simulated and observed E^* have a self-similar shape in the range $f_s < f < 2f_s$, which is usually called an equilibrium range of a wave spectrum (Phillips 1985). Second, the shape of the simulated wave spectrum for $f > f_s$ is similar to the observations. The f^{-4} dependence in the simulated spectra $E(f)$ is achieved by using the constant steepness spectrum ($a_i k_i =$ const.) in which $E(f) \sim a_i^2 \sim k_i^{-2}$ and $k_i^{-2} \sim f^{-4}$ from the linear dispersion relation for deep water waves. However, in the field spectra there is much more energy at frequencies $f < f_s$ due to the presence of swell. Many field observations of the speed of visible whitecaps have shown that the dominant speed of breaking waves is about half the phase speed of waves at the peak of the energy spectrum (Melville and Matusov 2002; Gemmrich et al. 2008; Thomson and Jessup 2009; Kleiss and Melville 2010; Schwendeman et al. 2014; Sutherland and Melville 2013). Assuming linear dispersion, this means that the frequency associated with breaking waves f_b is noticeably larger than the peak frequency f_p, and that f_b is usually in the equilibrium range. Thus

Accepted for publication in *Journal of Physical Oceanography*. DOI 10.1175/JPO-D-19-0138.1.

H_{eq} will be an appropriate choice for a characteristic height of visible breaking waves. Further, since H_{eq} is not sensitive to the amount of energy of swell waves, which is completely absent in our numerical simulations, it is preferable for the purpose of model-field observations comparisons of vertical scaling of turbulence dissipation rates. Here, H_{eq} prior to breaking onset is 0.24m, 0.20m, and 0.14m in the simulated cases T1, T2, and T3 respectively, with $H_{eq}/H_s \approx 0.8$ because the main part of the wave energy is distributed in the range $f_s < f < 2f_s$ (see Figure 1b).

Figure 1c shows that H_{eq} as defined in Eq. (7) varies between 0.45 and 0.7 of the corresponding significant wave height H_s for the field conditions with $6 < U_{10} < 16$ m/s. Considering the Pierson-Moskowitz spectrum, we obtain $f_s = 1.3 f_p$ and $H_{eq}/H_s = 0.57$ which is consistent with the averaged value of $H_{eq}/H_s \approx 0.6$ obtained from the observations of Schwendeman and Thomson (2015) and Thomson et al. (2016) in the North Pacific.

We define the active breaking index $I(x,y,t)$ as

$$I(x,y,t) = \mathscr{H}\left[\alpha^b_{sa}(x,y,t) - \alpha^b_{th}\right], \tag{8}$$

where $\mathscr{H}$ is the Heaviside step function, α^b_{sa} is the vertical average of the bubble void fraction over the surface layer of depth $d_s = 0.4H_{eq}$, and α^b_{th} is a threshold value. Then, we obtain the fraction of the active breaking crests, or active whitecap coverage, W_A of the breaking events occur between time t_1 and t_2 and over the area $\mathscr{A}$ as

$$W_A = \frac{\int_{t_1}^{t_2}\int_{-y_1}^{y_1}\int_{x_1}^{x_2} I \, dx\, dy\, dt}{\mathscr{A}\,(t_2 - t_1)}, \tag{9}$$

where x_1, x_2, y_1 indicate the horizontal extent of the averaging area $\mathscr{A} = 2y_1(x_2 - x_1)$ and are set such that it includes the breaking crests. Unless stated otherwise, we set $t_1 = t_0$ and $t_2 = t_0 + N_E T_g$ to do the time averaging over all available breaking events in the virtual tank after $t = t_0$. In the field, W_A (and W) is obtained from image processing of visible whitecaps and should be independent of the selected field of view. In Eq. (9), however, W_A depends on $\mathscr{A}$. As we will

Accepted for publication in *Journal of Physical Oceanography*. DOI 10.1175/JPO-D-19-0138.1.

explain later in this paper, choosing $\alpha_{th}^{b} = 0.02$ provides estimates of W_A which are consistent with the observed values of whitecap coverage in the open ocean (Schwendeman and Thomson 2015). We note that if d_s varies between $0.2H_{eq}$ and $0.6H_{eq}$ the corresponding W_A values vary less than 30% of the W_A value estimated using $d_s = 0.4H_{eq}$ for the simulated cases. Finally, the temporal variation of the instantaneous W_A values using Eq. (9) for the various individual simulated breakers (not shown) are consistent with the data reported in Figure 1 of Callaghan et al. (2016).

d. Conversion of the model results to virtual drifters

In this paper, our main goal is to examine potential sampling biases and convergence of statistics of the field observations of intermittent wave breaking turbulence collected by surface following platforms (*e.g.*, SWIFT drifters) using our high resolution numerical simulations. To do this, we need to sample our model results, which are available at fixed Eulerian grid points, in a manner which is similar to how a physical drifter (Figure 1f) obtains samples in the field.

We first introduce a number of virtual drifters that move with the free surface and local liquid velocity in the computational domain. Then, we interpolate the model Eulerian results onto vertical line segments that are attached to the virtual drifters and extend from the instantaneous free surface $z = \eta$ to $z = \eta - l_{vd}$. In the surface-following reference frame $z_{sf} = z - \eta$, all the interpolated results will be in the range $-l_{vd} < z_{sf} < 0$.

For each breaking event Em ($m = 1, 2, \ldots, N_E$), a total number of 231 virtual drifters are released at $t = t_0 + (m-1)T_g$, which is well before the onset of the main breaking event Em, and remain in the water for a time T_g. We consider both uniform and random initial spacing of the virtual drifters to make sure that the resultant statistics are independent of the initial deployment of the virtual drifters. Figure 1d,e show two snapshots of the instantaneous locations of the virtual drifters (markers) released uniformly at $x^* = -0.2, -0.5 < y^* < 0.5$ for the breaking events E3 and E4 of

Accepted for publication in *Journal of Physical Oceanography*. DOI 10.1175/JPO-D-19-0138.1.

the case T1. Figure 1f shows a snapshot of a physical drifter in the field in the vicinity of an active breaking crest propagating towards the drifter.

The horizontal location of each virtual drifter is updated using the vertical average of the water horizontal velocity components over the surface layer of depth $0.2H_{eq}$. Panels (g) and (h) show the corresponding horizontal displacements of some of the virtual drifters released in a uniform grid and during the events E3 and E4 of the case T1 respectively. Panel (i) shows an example of the horizontal displacement of a SWIFT drifter in the field. In these frames, each color segment represents the horizontal displacement during a fixed time, equal to T_s in the model results and $T_p/2$ in the observations. Both simulated and observed results indicate that a drifter trapped in an active breaking crest may experience horizontal displacements that are significantly greater than when it is riding on a non-breaking crest. This is consistent with the recent work of Deike et al. (2017b); Pizzo et al. (2019).

3. Results

A glossary of all variables used hereafter is given in Table A1 in the appendix. In our model results, the rate of transfer of energy from the resolved motions to the SGS motions is $\varepsilon_{sgs} = \nu_{sgs}|\mathscr{S}|^2$ where ν_{sgs} is the SGS eddy viscosity, $|\mathscr{S}|^2 = 2\mathscr{S}_{ij}\mathscr{S}_{ij}$, and $\mathscr{S}_{ij} = \frac{1}{2}(\partial\tilde{u}_i/\partial x_j + \partial\tilde{u}_j/\partial x_i)$ is the resolved rate of strain. ε_{sgs} includes both shear- and bubble-induced dissipation (Derakhti and Kirby 2014a). At high Reynolds number, with the filter width much larger than the Kolmogorov length scale, the viscous dissipation rate is typically much smaller than ε_{sgs}, and thus ε_{sgs} approximates the turbulent kinetic energy (TKE) dissipation rate ε, which is commonly considered as a characteristic indicator of intensity of turbulence.

Figure 2 shows two snapshots of 3-D variation of ε_{sgs} during active breaking period and $\approx 2T_s$ after the breaking-onset for the breaking event E3 of the case T1. Consistent with previous wave

Accepted for publication in *Journal of Physical Oceanography*. DOI 10.1175/JPO-D-19-0138.1.

breaking simulations (see, for example, Derakhti and Kirby 2014a, Figures 11 and 12), our numerical results indicate that wave-breaking-induced ε_{sgs} has a strong temporal and spatial variation, with local values of ε_{sgs} varying from $O(1)$ m^{2}s^{-3} (or W/kg) down to the background levels, and with large values of ε_{sgs} concentrated near the wave crest and in regions of high void fraction (bubble void fractions are not shown here). The latter is consistent with the recent laboratory measurements of turbulence dissipation rates ε within wave breaking crests by Deane et al. (2016). They reported large values of $\varepsilon > 1$ W/kg during the acoustically active phase of wave breaking in which air is actively entrained and fragmented into bubbles.

As summarized in §1, in most practical applications the long-time-average (*e.g.*, over many wave periods) of TKE dissipation rates over a relatively large surface area, $O(100L_p \times 100L_p)$, is of interest. In this section, we first examine how the Eulerian averages of ε_{sgs} compare with those obtained from surface following virtual drifters. Then we comment on the convergence of statistics obtained from the virtual drifters. Last, we examine the effect of incomplete sampling of ε_{sgs} by the virtual drifters due to limited vertical field of view and occlusion due to the entrained bubbles.

a. Lagrangian vs Eulerian averaging of ε_{sgs}

Figure 3a shows the spatio-temporal variation of the horizontal average of ε_{sgs} in a surface-following reference frame, $\breve{\varepsilon}_{sgs}(t, z_{sf})$, for the breaking event E3 of the case T1. Here, the averaging is performed over a surface that is parallel to $\eta(x,y,t)$ at a distance $|z_{sf}|$ below the free surface with the horizontal area of $2L_s \times L_s$. The values of $\breve{\varepsilon}_{sgs}$ before the breaking onset ($t/T_s < 133$) and those after $4T_s$ after the breaking onset ($t/T_s > 137$) are approximately comparable, demonstrating that the elevated turbulence dissipation rates due to a wave breaking event return to background levels after a few local wave periods. Figure 3b demonstrates the same trend in the depth in-

Accepted for publication in *Journal of Physical Oceanography*. DOI 10.1175/JPO-D-19-0138.1.

tegrated values of $\check{\varepsilon}_{sgs}$. Here the first two peaks are corresponding to the main breaking wave and the successive smaller breaking wave that occur in $133 < t/T_s < 134$ and $134 < t/T_s < 135$ respectively.

Figure 3c,e show the spatio-temporal variation of ε_{sgs} sampled by the two virtual drifters shown in Figure 2 during E3 of the case T1. Their corresponding time-averaged profiles, over $T_g \approx 9.5T_s$, in the surface-following reference frame are shown by the thick black lines in the panels (d) and (f), where the background thin gray lines represent the results from all available virtual drifters released before the beginning of the breaking event T1-E3. The considerable variation in $\overline{\varepsilon}_{sgs}$ obtained from virtual drifters indicates that, in the presence of surface wave breaking, the Lagrangian-based values of dissipation rates averaged over approximately 10 wave periods still have a considerable variation depending on the time fraction that a drifter is positioned within the localized turbulence patches generated during the active breaking process. We will examine the convergence of Lagrangian-averaged dissipation rates in the next section.

Figure 4a shows examples of the ensemble-averaged profiles of time-averaged dissipation rate $\overline{\overline{\varepsilon}}^{L}$, which are obtained from the Lagrangian virtual drifters (or time-averaging over many wave periods at least 1000 wave periods) as

$$\overline{\overline{\varepsilon}}^{L} = \frac{\Sigma_{i=1}^{i=231N_E}\overline{\varepsilon}_{sgs}^{i}}{231N_E}. \tag{10}$$

Here, $\overline{\varepsilon}_{sgs}^{i}$ is the time-averaged dissipation rate over time T_g sampled by the i^{th} $(i = 1,\ldots,231N_E)$ virtual drifter (Figure 3d,f). Figure 4a also shows examples of the ensemble-averaged profiles of the time-horizontal-averaged of the Eulerian model results $\overline{\overline{\varepsilon}}^{E}$ in the surface-following reference frame given by

$$\overline{\overline{\varepsilon}}^{E} = \frac{\Sigma_{m=1}^{m=N_E}\overline{\check{\varepsilon}}_{sgs}^{m}}{N_E}, \tag{11}$$

Accepted for publication in *Journal of Physical Oceanography*. DOI 10.1175/JPO-D-19-0138.1.

where $\overline{\varepsilon}^{m}_{sgs}$ is the time-horizontal-averaged dissipation rate over T_g of the breaking event E_m ($m = 1,\ldots,N_E$). Further, the corresponding profiles of $\overline{\overline{\varepsilon}}^{E}$ in the fixed reference frame is presented in the panel (b).

The vertical structure of the long-time-averaged turbulence dissipation rate $\overline{\overline{\varepsilon}}$ predicted by the model (Figure 4) has a number of important features. First our results indicate that $\overline{\overline{\varepsilon}}$ below a surface breaking layer with depth H_{eq} ($\approx 0.6H_s$) is proportional to $(-z_{sf}/H_{eq})^{-2}$ in the surface-following reference frame and $(-z/H_{eq})^{-2}$ in the fixed reference frame. This is consistent with the model proposed by Terray et al. (1996) (T96) in the fixed reference frame below the surface breaking layer with depth that T96 took to be $z > 0.6H_s$, and with more recent observations in a surface-following reference frame (Gemmrich 2010; Zippel et al. 2018; Sutherland and Melville 2015).

In contrast to T96, but consistent with the same recent field observations (Gemmrich 2010; Sutherland and Melville 2015; Thomson et al. 2016; Zippel et al. 2018), $\overline{\overline{\varepsilon}}$ is not constant in the surface breaking layer ($z < 0.6H_s$). Our model results indicate that in the upper half of the surface breaking layer in the surface-following reference frame, $|z_{sf}|/H_{eq} < 1/2$, $\overline{\overline{\varepsilon}}$ is well described with $\overline{\overline{\varepsilon}}(z_{sf} = 0)\exp(\beta z_{sf}/H_{eq})$ where β is a decreasing function of the active whitecap coverage W_A. In other words, $\overline{\overline{\varepsilon}}$ will be approximately constant for extreme wave breaking forcing with a relatively large value of W_A ($\gg 0.01$) for $|z_{sf}|/H_{eq} < 1/2$. Figure 4a also shows that $\overline{\overline{\varepsilon}}$ still follows the exponential decay in the lower half of the surface breaking layer $1/2 < |z_{sf}|/H_{eq} < 1$ with β increasing from approximately 8 for small W_A to 9 for large W_A values for the simulated cases.

Furthermore, in the fixed reference frame and within the surface breaking layer, $\overline{\overline{\varepsilon}}$ is described with $\overline{\overline{\varepsilon}}(z = 0)\exp(\beta z/H_{eq})$ where β is again a decreasing function of W_A but varies between 3 and 4 for the simulated cases. Our model results demonstrate that the Eulerian maximum of $\overline{\overline{\varepsilon}}$ is above $z = 0$, where $\overline{\overline{\varepsilon}}$ has persistently large values in $0 < z/H_{eq} < 1$ compared with those in other

Accepted for publication in *Journal of Physical Oceanography*. DOI 10.1175/JPO-D-19-0138.1.

z elevations. We note that Thomson et al. (2016) have reported a comparable vertical structure for $\overline{\overline{\varepsilon}}$ but with the Eulerian maximum slightly below $z = 0$ and the observed values of $\overline{\overline{\varepsilon}}$ in the fixed reference frame immediately started to decrease after reaching their maximum. We suspect that these differences between observed and simulated results are mainly due to the limitation of the experimental method in high bubble void fraction regions, and thus, the exclusion of high TKE dissipation rate values in the corresponding data. we will comment on further effects of this issue in §3.c below.

In addition to the vertical distribution of $\overline{\overline{\varepsilon}}$, the depth-integrated turbulence dissipation rate $\int \overline{\overline{\varepsilon}} dz$ ($= \int \overline{\overline{\varepsilon}} dz_{sf}$) is of significant interest, and as reviewed in §2.c, its relationship with the whitecap coverage W (or W_A) remains an active area of research with important impacts for wave prediction modeling, air-sea interaction, and ocean engineering communities. Figure 5a shows the variation of $\int \overline{\overline{\varepsilon}} dz$ with the active whitecap coverage W_A (Eq. 9) for our model results. As reviewed by Brumer et al. (2017), recent observations reveal that W is an increasing function, with the scatter of data, of the wind speed U_{10}; varies between 10^{-3} and 0.1 for $7 < U_{10} < 20$ m/s. Further, available data of active whitecap coverage $W_A = \lambda W$ ($\lambda < 1$) indicates that λ is a decreasing function, with the scatter of data, of U_{10}; varies between 0.5 ± 0.25 and 0.2 ± 0.1 for $5 < U_{10} < 20$ m/s (Scanlon and Ward 2016, Figure6.b). Thus the resulting values of $8 \times 10^{-4} < W_A < 0.021$ shown in 5a, after dividing by the correction factor λ, are comparable with the range of observed W values for $7 < U_{10} < 20$ m/s. Thus we conclude that our definition of W_A (Eq. 9) may be interpreted as an active part of the whitecap coverage values reported in the literature, and that the energetics of wave breaking forcing in the simulated cases may be comparable to most of the available field observations including Schwendeman and Thomson (2015); Thomson et al. (2016).

Accepted for publication in *Journal of Physical Oceanography*. DOI 10.1175/JPO-D-19-0138.1.

Assuming a power-law relationship

$$\int [\overline{\overline{\varepsilon}} - \overline{\overline{\varepsilon}}_0] dz_{sf} = aW_A^b, \tag{12}$$

where ε_0 is the background turbulence dissipation rate due to mechanisms other than visible wave breaking, $\varepsilon_0 \approx 0$ in our simulations. Using least squared curve fitting, we obtain $a = 0.077(-0.026, +0.039)$ and $b = 0.94(\pm 0.07)$ (with $R^2 = 0.98$), where coefficients in parentheses represent 95% confidence intervals. This is an interesting and important result, and we will further comment on it in §4.

Figure 5b shows that a relatively high fraction of total dissipation rate occurs above the mean sea level. This fraction is still noticeably high, $\approx 80\%$, even for small W_A values of about 0.001. This is consistent with the field observations of Gemmrich (2010) showing that most of the breaking turbulence is concentrated very close to the surface, especially in the wave crest. This is also consistent with the laboratory study of Deane et al. (2016), who found that relatively high dissipation rate values are concentrated in the crest region of the breaking waves. In particular, Deane et al. (2016) find that the majority of energy dissipation occurs within bubble plumes, where turbulent dissipates saturate around 10^0 or 10^1 m^{2}s^{-3}.

Finally, the results shown in Figure 4a and Figure 5 demonstrate that the Lagrangian statistics of intermittent wave breaking turbulence, obtained from the sampled data by freely drifting platforms, are representative of the corresponding Eulerian statistics when the length of the Lagrangian data is very large compared with the local wave breaking period. In the next section, we examine how such Lagrangian statistics converge as a function of the length of data.

Accepted for publication in *Journal of Physical Oceanography*. DOI 10.1175/JPO-D-19-0138.1.

b. Convergence of statistics

In this section, we examine how the Lagrangian statistics of dissipation rates obtained from n randomly selected virtual drifters $\overline{\overline{\varepsilon}}_n^L$ compare to the associated statistics using all available virtual drifters $\overline{\overline{\varepsilon}}^L$ (Eq. 10). We note that the normalized length of the considered data $\mathscr{L}/T_s$ used to obtain $\overline{\overline{\varepsilon}}_n^L$ and $\overline{\overline{\varepsilon}}^L$ are $\approx 9.5n$ and $\approx 9.5 \times 231 N_E$ respectively.

Figure 6 shows $\overline{\overline{\varepsilon}}_n^L$ (solid lines) for three n values and two different W_A as well as the corresponding ensemble-averaged profiles using all the virtual drifters $\overline{\overline{\varepsilon}}^L$ (dashed lines). The random selection of n virtual drifters for each n value were repeated 100 times (gray lines). For better visibility, five examples of these profiles are plotted as individual black curves. As expected for both cases, $\overline{\overline{\varepsilon}}_n^L$ (solid lines) converges to $\overline{\overline{\varepsilon}}^L$ (dashed lines) with increasing n or the length of signal. However, the convergence of statistics with increasing n occurs more rapidly for the case with a larger W_A value (or more active breaking) compared with the case with a relatively smaller W_A value.

Figure 7a shows the variation of the normalized RMSE of $\int \overline{\overline{\varepsilon}}_n^L dz_{sf}$ (with mean value $\int \overline{\overline{\varepsilon}}^L dz_{sf}$) with normalized signal length $\mathscr{L}/T_s \approx 9.5n$ for the two cases shown in Figure 6. The results show that this error may be fairly reasonably estimated using the Gaussian distribution formulation (dashed lines). Further, Figure 7b shows the variation of the normalized standard error for four values of $\mathscr{L}/T_s = 100, 500, 1000$ and 3000 for all W_A values. Our results suggest that the required length of data to obtain stable Lagrangian statistics (with normalized RMSE $< 25\%$) of intermittent wave-breaking-induced turbulence using freely drifting platforms should be at least 1000 and 3000 characteristic wave breaking periods for medium to high sea states (*e.g.*, $W_A > 5 \times 10^{-3}$) and low sea states (*e.g.*, $W_A < 5 \times 10^{-3}$) respectively. In other words, more Lagrangian sampled data

Accepted for publication in *Journal of Physical Oceanography*. DOI 10.1175/JPO-D-19-0138.1.

is needed to obtain stable statistics of wave breaking turbulence as the probability of breaking or W_A decreases.

Assuming the characteristic wave breaking period of sea waves as $T_p/2$ (see §2.c), the minimum required length of data to perform averaging will be $\mathscr{L}_{min} = 500T_p$ and $1500T_p$ for $W_A > 5\times10^{-3}$ and $W_A < 5\times10^{-3}$ respectively. In other words, $\mathscr{L}_{min}$ varies between 1 to 3 hours depending on a particular sea state. Brumer et al. (2017) and Callaghan and White (2009) found that whitecap data collected over approximately 20 to 30 minutes are needed to reduce uncertainty related to average whitecap coverage values. We note that $\mathscr{L}_{min}$ may be obtained from one or multiple drifters, with a sampling time of each drifter should be smaller than the time-scale during which the wind forcing condition can be assumed as constant. We will show in §4 that considering $\mathscr{L}_{min}$ noticeably decreases the amount of scatter in the previous observations of the total TKE dissipation rates.

c. Effects of occlusion due to the entrained bubbles and truncated vertical sampling

We know from previous numerical (Derakhti and Kirby 2014a) and laboratory (Blenkinsopp and Chaplin 2007) studies that the most active region of turbulence generation and dissipation include relatively large air bubble void fractions. Figure 8a shows the distribution of the number of the simulated data points sampled by the virtual drifters across dissipation rate and bubble void fraction bins, that are uniformly spaced in log scale, for the breaking event E3 of the case T1. The results indicate that $\alpha^b > 1\%$ in a noticeable portion of regions with relatively high ε_{sgs} values. Figure 8b shows examples of the variation of the fraction of the total dissipation within the regions with $\alpha^b < \alpha^b_0$ against α^b_0. In other words, although the high dissipation regions occur in a short portion of time ($\sim W_A$) but their contribution to the total dissipation is large. The results shown in Figure 8 reveal that approximately half of the total dissipation occur in regions with $\alpha^b > 1\%$.

Accepted for publication in *Journal of Physical Oceanography*. DOI 10.1175/JPO-D-19-0138.1.

Void fractions above 1% significantly decrease the quality of the data collected by acoustic Doppler methods by decreasing the correlation of coherent pulses (Mori et al. 2007). As a result, a large portion of high dissipation rate values (Figure 8b) in the observed data are occluded by bubbles. Figure 9a shows the comparison between the vertical profiles of averaged dissipation rates obtained by (solid lines) a regular ensemble-time-averaging defined in (10) and (dashed lines) a conditional averaging over data points with $\alpha^b < 1\%$ for the two cases with different W_A values. Although the effect of the occlusion due to bubbles is limited to the breaking surface layer $|z_{sf}| < 0.6H_{eq}$, such data occlusion results in a considerable under-prediction of the total wave breaking dissipation rates in field observations using acoustic Doppler methods. Further, a limited vertical extend of sampled data by drifters causes the underestimation of the total dissipation rates as well.

If we assume that a drifter can only sample the TKE dissipation rates in regions with $\alpha^b < \alpha_0^b$ and up to a depth $|z_0|$, then the incomplete observed wave-breaking-induced TKE dissipation rates, $\int_{z_0}^{0} [\overline{\overline{\varepsilon}} - \overline{\overline{\varepsilon}}_0]_{\alpha^b < \alpha_0^b}\, dz_{sf}$, will be always less than their corresponding true values $\int [\overline{\overline{\varepsilon}} - \overline{\overline{\varepsilon}}_0]\, dz_{sf}$ (Eq. 12).

Figure 9b shows examples of the variation of a correction factor $\mathscr{C} > 1$ defined as

$$\mathscr{C} = \frac{\int [\overline{\overline{\varepsilon}} - \overline{\overline{\varepsilon}}_0]\, dz_{sf}}{\int_{z_0}^{0} [\overline{\overline{\varepsilon}} - \overline{\overline{\varepsilon}}_0]_{\alpha^b < \alpha_0^b}\, dz_{sf}}, \tag{13}$$

with the depth and the active whitecap coverage W_A for $\alpha_0^b = 1\%$. As expected, $\mathscr{C}$ is an increasing function of W_A and a decreasing function of $|z_0|$. However, $\mathscr{C}$ has a very weak correlation with $|z_0|$ for $|z_0| > 0.6H_{eq}$ (or below a breaking surface layer). Based on our numerical results, we obtain a simple relationship to predict $\mathscr{C}$ as a function of W_A and $|z_0|/H_{eq}$:

$$\mathscr{C} \approx \mathscr{C}_b\, Z^{\gamma} \tag{14}$$

where $Z = \mathrm{Min}(|z_0|/H_{eq}, 0.6) + 0.4$,

$$\mathscr{C}_b = c_1 \log_{10} W_A + c_2, \tag{15}$$

Accepted for publication in *Journal of Physical Oceanography*. DOI 10.1175/JPO-D-19-0138.1.

and

$$\gamma = d_1 \log_{10} W_A + d_2. \tag{16}$$

Here the empirical coefficients c_1, c_2, d_1, and d_2 are obtained for a particular choice of α_0^b and by using the least squared curve fitting. Table 2 documents these parameters for $\alpha_0^b = 1/3, 1$, and 3%.

The two line segments with markers shown in Figure 9b represent the corresponding fits given in Eqs.(14-16) (here $\alpha_0^b = 1\%$) for the smallest and largest W_A values of the simulated cases. We conclude that the empirical formulations Eqs. (14-16) provide a fairly reasonable approximation for the correction factor $\mathscr{C}$ for the range of W_A considered here.

4. Discussion

These results (§3.b and §3.c) improve interpretation of observed long-time-averaged total wave-breaking-induced TKE dissipation rates, $\int[\overline{\overline{\varepsilon}} - \overline{\overline{\varepsilon}}_0]dz_{sf}$. However, they are purely based on the idealized wave forcing and boundary conditions. Further, there is some uncertainty in generalizing our results to a broader range of field observations, *e.g.*, using the correction factor $\mathscr{C}$ (Eqs. 14-16). Proper application of the model results to field data relies on the connection between the model active whitecap coverage defined in Eq. (9) and field estimates of active whitecap coverage using image processing techniques.

Here, we examine the variation of the corrected total wave-breaking-induced TKE dissipation rates

$$\int[\overline{\overline{\varepsilon}} - \overline{\overline{\varepsilon}}_0]dz_{sf} \approx \mathscr{C} \int_{z_0}^{0} [\overline{\overline{\varepsilon}} - \overline{\overline{\varepsilon}}_0]_{\text{Obs}} dz_{sf} \tag{17}$$

against the corresponding observed whitecap coverage W provided by Schwendeman and Thomson (2015) and the rate of wind energy input examined by Thomson et al. (2016). Schwendeman and Thomson (2015) provided 119 data points including the whitecap coverage W estimated from shipboard video systems, the total observed TKE dissipation rate $\int_{z_0}^{0}[\overline{\overline{\varepsilon}} - \overline{\overline{\varepsilon}}_0]_{\text{Obs}} dz_{sf}$ with

Accepted for publication in *Journal of Physical Oceanography*. DOI 10.1175/JPO-D-19-0138.1.

$|z_0| = 0.42$m, wave spectra parameters, wind speed U_{10} and air-side friction velocity u_*. Here $\int_{z_0}^{0}[\overline{\overline{\varepsilon}} - \overline{\overline{\varepsilon}}_0]_{\text{Obs}} dz_{sf}$ is the observed TKE dissipation rate values above a background level and is collected from the freely drifting SWIFT drifters (Thomson 2012). Following the results presented in §3.b, we also consider clustering of the observed data to obtain averaged values over at least one hour, in addition to applying the correction $\mathscr{C}$ on the observed data.

To estimate $\mathscr{C}$, we need to estimate the active whitecap coverage W_A from the observations of W provided by Schwendeman and Thomson (2015), where $W_A = \lambda W$ and λ ranges from 0.5 ± 0.25 to 0.2 ± 0.1 in moderate to high sea states (Scanlon and Ward 2016, Figure 6b). We use a fit, provided by Callaghan (2018), to the bin-averaged λ measurements of Scanlon and Ward (2016) given by

$$\lambda = \frac{1}{1 + 8.65\,[0.001U_{10}^2 + 0.02]^{0.69}}, \tag{18}$$

in which the estimated λ values decreases from ≈ 0.5 for $U_{10} = 5$ m/s to ≈ 0.15 for $U_{10} = 23$ m/s (for further details see Callaghan 2018, Figure 5a and the related text therein).

a. Observed TKE dissipation rates versus active whitecap coverage

Figure 10 shows the variation of $\int_{z_0}^{0}[\overline{\overline{\varepsilon}} - \overline{\overline{\varepsilon}}_0]_{\text{Obs}} dz_{sf}$ (denoted by small circles) and $\mathscr{C}\int_{z_0}^{0}[\overline{\overline{\varepsilon}} - \overline{\overline{\varepsilon}}_0]_{\text{Obs}} dz_{sf}$ (denoted by small diamonds) with W (panel a) and with $W_A = \lambda W$ (panel b) for all available data points, where ε_0 represents turbulence dissipation by any mechanisms other than visible whitecaps, e.g., micro-breakers, Langmuir circulations, internal breaking waves, shear production, etc. In general, the background turbulence dissipation rate per unit surface area (or $\int[\overline{\overline{\varepsilon}}_0]_{\text{Obs}} dz_{sf}$) is a sea state dependent quantity, and may vary between $O(0.01)$ W/m^2 (Hwang and Sletten 2008) and $O(0.1)$ W/m^2 (Gemmrich 2010; Sutherland and Melville 2015). Here, we take $\int_{z_0}^{0}[\overline{\overline{\varepsilon}}_0]_{\text{Obs}} dz_{sf} = 3.2 \times 10^{-4}[\text{m}^3\text{s}^{-3}]$ (≈ 0.3W/m^2) which is approximately 0.9 of the minimum observed $\int_{z_0}^{0}[\overline{\overline{\varepsilon}}]_{\text{Obs}} dz_{sf}$ value reported by Schwendeman and Thomson (2015). Applying our

Accepted for publication in *Journal of Physical Oceanography*. DOI 10.1175/JPO-D-19-0138.1.

correction factor $\mathscr{C}$ (Eqs. 14-16) significantly improves the results, such that the variation of the total TKE dissipation rates increases approximately one order of magnitude by increasing W from $\approx 10^{-3}$ to $\approx 3\times10^{-2}$. Such strong correlation between $\int[\overline{\overline{\varepsilon}} - \overline{\overline{\varepsilon}}_0]dz_{sf}$ and W, or W_A, is consistent with our simulation results presented in Figure 5a and with previous semi-empirical and field studies (Hwang and Sletten 2008; Anguelova and Hwang 2016; Callaghan 2018).

Based on the results shown in §3.b, part of the scatter in the data shown in Figure 10 (small symbols) may be related to an insufficient record length $\mathscr{L}$ (here $\mathscr{L} = 512\text{s} \approx 40-80T_p$) used to perform the averaging, especially for W values smaller than 5×10^{-3}. We first sort the data points corresponding to developing ($c_p \leq U_{10}$) and developed ($c_p > U_{10}$) sea states into U_{10} bins with a spacing of 1 m/s. Then we remove the data points in which the measured W values vary from the threshold power law fit provided by Callaghan et al. (2008) by more than a factor of 3. Finally, the associated average values of different parameters are calculated using the remaining data points at each bin with enough data points such that $\mathscr{L} > 400\hat{T}_p$, hereafter $\hat{()}$ represent clustered averaging within each U_{10} bin.

Performing the clustered averaging described above on the data set of Schwendeman and Thomson (2015) results in seven clustered data points with $\hat{U}_{10} = 8.2, 8.8, 10.0, 11.2, 15.0$ and 15.9 m/s, all characterized as a developed sea state. The corrected and raw clustered averaged values are denoted by large symbols in Figure 10, where the size and color of the corrected data points represent their relative $\mathscr{L}/\hat{T}_p$ and the wave age values respectively. Further, the range of the observed W values for each bin is denoted by the vertical line segment in Figure 10a. The horizontal line segments represent sensitivity of the results with respect to $0.1 < \lambda < 0.75$. Finally, the small gray diamonds show the sensitivity of the corrected clustered-averaged total dissipation rates with respect to the variation of the resulting correction factor $\mathscr{C}$ for the choice of $\alpha_0^b = 1/3\%$ and 3%.

Accepted for publication in *Journal of Physical Oceanography*. DOI 10.1175/JPO-D-19-0138.1.

Using least-squared curve fitting, and assuming a power-law relationship

$$\int [\overline{\overline{\varepsilon}} - \overline{\overline{\varepsilon}}_0] dz_{sf} = a_1' W^{b_1'} = a_1 W_A^{b_1}, \qquad (19)$$

we obtain $a_1' = 0.026(-0.012, +0.022)$ and $b_1' = 0.77(\pm 0.12)$ (with $R^2 = 0.98$) and $a_1 = 0.24(-0.17, +0.58)$ and $b_1 = 0.98(\pm 0.2)$ (with $R^2 = 0.97$), where coefficients in parentheses represent 95% confidence intervals. Both our simulation results (Figure 5a) and the corrected clustered-averaged observations (Figure 10b) suggest that the total wave-breaking-induced TKE dissipation rates $\int [\overline{\overline{\varepsilon}} - \overline{\overline{\varepsilon}}_0] dz_{sf}$ have a power law dependence with W_A with the exponent slightly less than 1. Thus, the empirical relationship between total dissipation and whitecap coverage is approximately linear.

Dynamical explanations for the whitecap coverage dependence are proposed by Callaghan (2018), who scales dissipation rates with the volume of bubble plumes caused by breaking waves (and thereby the active whitecap coverage and bubble plume penetration depth). In particular, results with a fixed averaged bubble penetration depth in Figure 8 of Callaghan (2018) show a similar dependence in comparison to Figures 5a and 10b in the present work. Anguelova and Hwang (2016) also demonstrate a relation between active whitecap coverage and total wave breaking dissipation rates. We further comment on this in the next section. Quantification of averaged penetration depth of bubble plumes relative to active whitecap areas is left for future study.

b. Dissipation scaling and the distribution of breaking crests

Many previous studies (e.g., Melville and Matusov 2002; Thomson and Jessup 2009; Romero et al. 2012; Sutherland and Melville 2013) have applied the Phillips (1985) framework to estimate an energy dissipation rate using the fifth moment of the breaking crest-length distribution $\Lambda(c)$,

Accepted for publication in *Journal of Physical Oceanography*. DOI 10.1175/JPO-D-19-0138.1.

where c is the crest speed, as

$$\int [\overline{\overline{\varepsilon}} - \overline{\overline{\varepsilon}}_0] dz_{sf} = \frac{\rho b}{g} \int c^5 \Lambda(c) dc. \tag{20}$$

Although the present study lacks measurements of $\Lambda(c)$, the results herein are still relevant to the scaling of the breaking dissipation rate and the breaking strength parameter b. Beginning with the laboratory work of Drazen et al. (2008), the emerging literature suggests a dependence $b \sim (Ak)^{5/2}$, where Ak is the wave steepness given by amplitude A and wavenumber k. Romero et al. (2012) extended this from the steepness of wave packets in the laboratory to the spectral steepness, such that dissipation could be prescribed in a spectral wave model. Zappa et al. (2016) recently reviewed the published results on the breaking strength parameter b.

Although we do not evaluate a spectral dissipation rate or the breaking strength with the present analysis, we can attempt to reconcile the $\Lambda(c)$ framework with the relationship between the total dissipation rate and active whitecap coverage. Kleiss and Melville (2010) relate active whitecap coverage W_A to the first moment of $\Lambda(c)$ and a timescale for the persistence of the breaking crest τ,

$$W_A = \int c\tau\Lambda(c) dc. \tag{21}$$

If the timescale τ is proportional to breaking wave period T, then dispersion implies it is proportional to phase speed and the effective relation is active whitecap coverage and the second moment, $W_A = \int c^2 \Lambda(c) dc$. Kleiss and Melville (2010) evaluated these formulations, along with the zeroth moment of $\Lambda(c)$, and find that all have strong linear relations ($R^2 > 0.96$) to the observed active whitecap coverage (their Figure 7). If these lower moments of $\Lambda(c)$ are all similarly related to W_A, we can expect higher moments to be related as well. Generally, for a narrow distribution, higher moments have a quasi-linear relationship to lower moments, because the tail of the distribution is sufficiently small as to have minimal effect. Given the canonical tail of $\Lambda(c) \sim c^{-6}$ (Melville

Accepted for publication in *Journal of Physical Oceanography*. DOI 10.1175/JPO-D-19-0138.1.

and Matusov 2002), the distribution is indeed narrow and the net dependence of total dissipation is closer to c^{-1}.

The implications for spectral dissipation remain to be determined, but it is thus at least empirically consistent for both active whitecap coverage W_A (Figures 5a and 10b) and $\int c^5\Lambda(c)dc$ to be related to the total wave breaking dissipation rate.

c. Observed TKE dissipation versus wind energy input rates

In an equilibrium sea state, the rate of wind energy input per unit area to the upper ocean F (m^3s^{-3} or W/kg) is balanced mainly by the wave breaking energy dissipation. Figure 11 demonstrates the significance of applying our correction factor $\mathscr{C}$ to the data from Thomson et al. (2016) in observing this expected equilibrium balance. In addition, the results show that clustering of the individual data points (to achieve long enough record lengths $\mathscr{L}$) noticeably reduces the scatter. Here, we use the formulation $F = c_e u_*^2 \rho^a/\rho$, where ρ^a is a constant air density. Other formulations for the wind input rate give similar results (see Thomson et al. (2016)). The vertical and horizontal line segments represent sensitivity of the results with respect to $2 < c_e < 3$ and $0.1 < \lambda < 0.75$ respectively. As in Figure 10, the small gray diamonds show the sensitivity of the corrected clustered-averaged total dissipation rates with respect to the variation of the resulting correction factor $\mathscr{C}$ for the choice of $\alpha_0^b = 1/3\%$ and 3%.

Given equilibrium conditions in which wind input and breaking dissipation rates balance, it is not surprising that whitecap coverage has a nearly linear relationship to dissipation rate. Both whitecap coverage and wind input have been regularly related to the cube of the wind speed (e.g., Brumer et al. (2017)) or the cube of wind friction velocity (e.g., Craig and Banner (1994)). The implied empirical dependence between these parameters is thus linear, with dynamic interpretation still an open question.

Accepted for publication in *Journal of Physical Oceanography*. DOI 10.1175/JPO-D-19-0138.1.

5. Summary

A high-resolution two-fluid LES/VOF numerical model (Derakhti and Kirby 2014a) representing breaking waves and turbulence is used to show that robust estimates of average turbulence dissipation rates are possible from sparse Lagrangian sampling in a surface-following reference frame (as done with field observations). Bubbles are treated as a multi-component continuum, with different components representing different bubble diameters. Turbulence is modeled using LES with a dynamic Smagorinsky closure. Bubble contributions to dissipation and momentum transfer between the water and air phases are considered. Numerical simulations are run for many wave periods to build up quasi-steady background turbulence levels, with breaking events occurring approximately every $10T$, where T is the wave period. We sample the LES/VOF model results with a large number of virtual surface-following drifters that are initially distributed in the numerical domain, regularly or irregularly, before each breaking event. Time-averaged Lagrangian statistics are obtained using the time-series sampled by the virtual drifters.

Convergence of statistics occurs for signals that have minimum length of approximately $1000T$ with randomly spaced observations in time and space relative to 3-D breaking events. This result holds over a wide range of relative breaking activity, which is scaled in the model domain to match field observations of whitecap coverage. The average dissipation rates have a nearly linear relation to whitecap coverage. The model results also indicated that the high turbulence dissipation rates are correlated with bubble plumes (and thus high void fractions). Using a canonical cutoff of 0.01 void fraction ($\alpha^b = 1\%$) for field observations of turbulence, an empirical correction factor $\mathscr{C} = \mathscr{C}(W_A, |z_0|/H_{eq})$ is developed and applied to the previous observations of Thomson et al. (2016); where W_A is the active whitecap coverage, $|z_0|$ is the extent of measurements over depth, and H_{eq} is a characteristic breaking wave height.

Accepted for publication in *Journal of Physical Oceanography*. DOI 10.1175/JPO-D-19-0138.1.

Applying the correction factor to observations significantly alters the estimations of average turbulence dissipation rates sampled by surface following drifters, especially in high sea states, and thus, improves the inferred energy balance of wind input rates and turbulence dissipation rates. Finally, both our simulation results and the corrected observations suggested that the total wave breaking dissipation rates have a nearly linear relation with active whitecap coverage.

We emphasize that the proposed correction factor is based purely on numerical simulations of a limited number of idealized wave breaking events, in which a number of relevant processes such as direct wind forcing have been ignored. In the absence of new field methods for direct observation of turbulence inside bubble plumes, applying the proposed correction factor to the open ocean conditions must be made cautiously. More field observations of near-surface turbulence and bubble plumes are needed, especially in high sea states.

Acknowledgments. This work was supported by grants OCE-1756040 and OCE-1756355 from the US National Science Foundation. SWIFT data are available from www.apl.washington.edu/swift and whitecap coverage data are available from http://hdl.handle.net/1773/42596.

APPENDIX

A Summary of All Mathematical Variables and Symbols Used in §3-§5

Table A1 summarizes the symbols, definitions, and units for the variables used in the Results, Discussion and Summary sections.

References

Agrawal, Y., E. A. Terray, M. A. Donelan, P. A. Hwang, A. J. W. III, W. M. Drennan, K. Kahma, and S. A. Krtaigorodski, 1992: Enhanced dissipation of kinetic energy beneath surface waves.

Accepted for publication in *Journal of Physical Oceanography*. DOI 10.1175/JPO-D-19-0138.1.

Nature, **359**, 219–220, doi:10.1038/359219a0.

Anguelova, M. D., and P. A. Hwang, 2016: Using energy dissipation rate to obtain active whitecap fraction. *Journal of Physical Oceanography*, **46**, 461–481, doi:10.1175/JPO-D-15-0069.1.

Babanin, A. V., 2011: *Breaking and dissipation of ocean surface waves*. Cambridge Univ. Press.

Blenkinsopp, C. E., and J. R. Chaplin, 2007: Void fraction measurements in breaking waves. *Proc. Royal Soc. A: Math, Phys. Eng. Sci.*, **463**, 3151–3170, doi:10.1098/rspa.2007.1901.

Brumer, S. E., C. J. Zappa, I. M. Brooks, H. Tamura, S. M. Brown, B. W. Blomquist, C. W. Fairall, and A. Cifuentes-Lorenzen, 2017: Whitecap coverage dependence on wind and wave statistics as observed during so gasex and hiwings. *J Phys. Oceanogr.*, **47**, 2211–2235, doi: 10.1175/JPO-D-17-0005.1.

Callaghan, A., G. de Leeuw, L. Cohen, and C. D. O'Dowd, 2008: Relationship of oceanic whitecap coverage to wind speed and wind history. *Geophys. Res. Lett.*, **35 (23)**, doi:10.1029/2008GL036165.

Callaghan, A. H., 2018: On the relationship between the energy dissipation rate of surface-breaking waves and oceanic whitecap coverage. *J. Phys. Oceanogr.*, **48**, 2609–2626, doi: 10.1175/JPO-D-17-0124.1.

Callaghan, A. H., G. B. Deane, and M. D. Stokes, 2016: Laboratory air-entraining breaking waves: Imaging visible foam signatures to estimate energy dissipation. *Geophys. Res. Let.*, **43**, 11–320, doi:10.1002/2016GL071226.

Callaghan, A. H., G. B. Deane, and M. D. Stokes, 2017: On the imprint of surfactant-driven stabilization of laboratory breaking wave foam with comparison to oceanic whitecaps. *J. Geophys. Res.: Oceans*, **122**, 6110 – 6128, doi:10.1002/2017JC012809.

Accepted for publication in *Journal of Physical Oceanography*. DOI 10.1175/JPO-D-19-0138.1.

Callaghan, A. H., and M. White, 2009: Automated processing of sea surface images for the determination of whitecap coverage. *J. Atmos. Oceanic Tech.*, **26**, 383–394, doi:10.1175/2008JTECHO634.1.

Carrica, P. M., D. Drew, F. Bonetto, and R. T. Lahey, 1999: A polydisperse model for bubbly two-phase flow around a surface ship. *Int. J. Multiphase Flow*, **25**, 257–305, doi:10.1016/S0301-9322(98)00047-0.

Craig, P. D., and M. L. Banner, 1994: Modeling wave-enhanced turbulence in the ocean surface layer. *J. Phys. Oceanogr.*, **24**, 2546–2559, doi:10.1175/1520-0485(1994)024⟨2546:MWETIT⟩2.0.CO;2.

Deane, G. B., M. D. Stokes, and A. H. Callaghan, 2016: The saturation of fluid turbulence in breaking laboratory waves and implications for whitecaps. *J. Phys. Oceanogr.*, **46**, 975–992, doi:10.1175/JPO-D-14-0187.1.

Deike, L., L. Lenain, and W. K. Melville, 2017a: Air entrainment by breaking waves. *Geophys. Res. Let.*, 3779–3787, doi:10.1002/2017GL072883, 2017GL072883.

Deike, L., W. K. Melville, and S. Popinet, 2016: Air entrainment and bubble statistics in breaking waves. *J. Fluid Mech.*, **801**, 91–129, doi:10.1017/jfm.2016.372.

Deike, L., N. Pizzo, and W. K. Melville, 2017b: Lagrangian transport by breaking surface waves. *J. Fluid. Mech.*, **829**, 364–391, doi:10.1017/jfm.2017.548.

Derakhti, M., M. L. Banner, and J. T. Kirby, 2018: Predicting the breaking strength of gravity water waves in deep and intermediate depth. *J. Fluid Mech.*, **848**, doi:10.1017/jfm.2018.352.

Derakhti, M., and J. T. Kirby, 2014a: Bubble entrainment and liquid bubble interaction under unsteady breaking waves. *J. Fluid Mech.*, **761**, 464–506, doi:10.1017/jfm.2014.637.

Accepted for publication in *Journal of Physical Oceanography*. DOI 10.1175/JPO-D-19-0138.1.

Derakhti, M., and J. T. Kirby, 2014b: Bubble entrainment and liquid bubble interaction under unsteady breaking waves. Research Report CACR-14-06, Center for Applied Coastal Research, University of Delaware, available at http://www.udel.edu/kirby/papers/derakhti-kirby-cacr-14-06.pdf.

Derakhti, M., and J. T. Kirby, 2016: Breaking-onset, energy and momentum flux in unsteady focused wave packets. *J. Fluid Mech.*, **790**, 553–581, doi:10.1017/jfm.2016.17.

Derakhti, M., J. T. Kirby, M. L. Banner, S. T. Grilli, and J. Thomson, 2019: A unified breaking-onset criterion for surface gravity water waves in arbitrary depth. *J. Geophys. Res.*, **in preparation**.

Drazen, D., W. K. Melville, and L. Lenain, 2008: Inertial scaling of dissipation in unsteady breaking waves. *J. Fluid Mech.*, **611**, 307–332, doi:10.1017/S0022112008002826.

Esters, L., Ø. Breivik, S. Landwehr, A. ten Doeschate, G. Sutherland, K. H. Christensen, J.-R. Bidlot, and B. Ward, 2018: Turbulence scaling comparisons in the ocean surface boundary layer. *J. Geophys. Res.*, **123**, 2172–2191, doi:10.1002/2017JC013525.

Francois, M. M., S. J. Cummins, E. D. Dendy, D. B. Kothe, J. M. Sicilian, and M. W. Williams, 2006: A balanced-force algorithm for continuous and sharp interfacial surface tension models within a volume tracking framework. *J. Comput. Phys.*, **213**, 141–173, doi:10.1016/j.jcp.2005.08.004.

Gemmrich, J., 2010: Strong turbulence in the wave crest region. *J. Phys. Oceanogr.*, **40**, 583–595, doi:10.1175/2009JPO4179.1.

Accepted for publication in *Journal of Physical Oceanography*. DOI 10.1175/JPO-D-19-0138.1.

Gemmrich, J., T. Mudge, and V. Polonichko, 1994: On the energy input from wind to surface waves. *J. Phys. Oceanogr.*, **24**, 2413–2417, doi:10.1175/1520-0485(1994)024⟨2413:OTEIFW⟩2.0.CO;2.

Gemmrich, J. R., M. L. Banner, and C. Garrett, 2008: Spectrally resolved energy dissipation rate and momentum flux of breaking waves. *J. Phys. Oceanogr.*, **38**, 1296–1312, doi:10.1175/2007JPO3762.1.

Gemmrich, J. R., and D. Farmer, 2004: Near-surface turbulence in the presence of breaking waves. *J. Phys. Ocean.*, **34**, 1067–1086, doi:10.1175/1520-0485(2004)034⟨1067:NTITPO⟩2.0.CO;2.

Hwang, P. A., and M. A. Sletten, 2008: Energy dissipation of wind-generated waves and whitecap coverage. *J Geophys. Res.: Oceans*, **113 (C2)**, doi:doi:10.1029/2007JC004277.

Kirby, J. T., and M. Derakhti, 2019: Short-crested wave breaking. *European Journal of Mechanics/B Fluids*, **73**, 100–111, doi:10.1016/j.euromechflu.2017.11.001.

Kleiss, J. M., and W. K. Melville, 2010: Observations of wave breaking kinematics in fetch-limited seas. *J. Phys. Oceanogr.*, **40**, 2575–2604, doi:10.1175/2010JPO4383.1.

Lamarre, E., and W. Melville, 1991: Air entrainment and dissipation in breaking waves. *Nature*, **351**, 469–472.

Ma, G., F. Shi, and J. T. Kirby, 2011: A polydisperse two-fluid model for surf zone bubble simulation. *J. Geophys. Res.*, **116**, C05 010, doi:10.1029/2010JC006 667.

Melville, W. K., 1996: The role of surface-wave breaking in air-sea interaction. *Ann. Rev. Fluid Mech.*, **28**, 279–321.

Melville, W. K., and P. Matusov, 2002: Distribution of breaking waves at the ocean surface. *Nature*, **417**, 58–63.

Accepted for publication in *Journal of Physical Oceanography*. DOI 10.1175/JPO-D-19-0138.1.

Mori, N., T. Suzuki, and S. Kakuno, 2007: Noise of acoustic doppler velocimeter data in bubbly flows. *J. Eng. Mech.*, **133**, 122–125, doi:10.1061/(ASCE)0733-9399(2007)133:1(122).

Phillips, O. M., 1985: Spectral and statistical properties of the equilibrium range in wind-generated gravity waves. *J. Fluid Mech.*, **156**, 495–531, doi:10.1017/S0022112085002221.

Pizzo, N., W. K. Melville, and L. Deike, 2019: Lagrangian transport by nonbreaking and breaking deep-water waves at the ocean surface. *J. Phys. Oceanogr.*, **49**, 983–992, doi:10.1175/JPO-D-18-0227.1.

Rapp, R. J., and W. K. Melville, 1990: Laboratory measurements of deep-water breaking waves. *Phil. Trans R. Soc. Lond. A*, **331**, 735–800, doi:10.1098/rsta.1990.0098.

Romero, L., W. K. Melville, and J. M. Kleiss, 2012: Spectral energy dissipation due to surface wave breaking. *J. Phys. Oceanogr.*, **42**, 1421–1444, doi:10.1175/JPO-D-11-072.1.

Scanlon, B., and B. Ward, 2016: The influence of environmental parameters on active and maturing oceanic whitecaps. *J. Geophys. Res.*, **121**, 3325–3336.

Schwendeman, M., and J. Thomson, 2015: Observations of whitecap coverage and the relation to wind stress, wave slope, and turbulent dissipation. *J. Geophys. Res.: Oceans*, **120**, 8346–8363, doi:10.1002/2015JC011196.

Schwendeman, M., J. Thomson, and J. Gemmrich, 2014: Wave breaking dissipation in a young wind sea. *J. Phys. Oceanogr.*, **44**, 104–127, doi:10.1175/JPO-D-12-0237.1.

Sutherland, P., and W. K. Melville, 2013: Field measurements and scaling of ocean surface wave-breaking statistics. *Geophys. Res. Let.*, 3074–3079, doi:10.1002/grl.50584.

Accepted for publication in *Journal of Physical Oceanography*. DOI 10.1175/JPO-D-19-0138.1.

Sutherland, P., and W. K. Melville, 2015: Field measurements of surface and near-surface turbulence in the presence of breaking waves. *J. Phys. Oceanogr.*, **45**, 943–965, doi:10.1175/JPO-D-14-0133.1.

Terray, E., M. Donelan, Y. Agrawal, W. Drennan, K. Kahma, A. Williams, P. Hwang, and S. Kitaigorodskii, 1996: Estimates of kinetic energy dissipation under breaking waves. *J. Phys. Oceanogr.*, **26**, 792–807, doi:10.1175/1520-0485(1996)026⟨0792:EOKEDU⟩2.0.CO;2.

Thomson, J., 2012: Wave breaking dissipation observed with SWIFT drifters. *Journal of Atmospheric and Oceanic Technology*, **29**, 1866–1882, doi:10.1175/JTECH-D-12-00018.1.

Thomson, J., and A. Jessup, 2009: A fourier-based method for the distribution of breaking crests from video observations. *J. Atmos. Ocean. Tech.*, **26**, 1663–1671, doi:10.1175/2009JTECHO622.1.

Thomson, J., M. S. Schwendeman, S. F. Zippel, S. Moghimi, J. Gemmrich, and W. E. Rogers, 2016: Wave-breaking turbulence in the ocean surface layer. *J. Phys. Oceanogr.*, **46**, 1857–1870, doi:10.1175/JPO-D-15-0130.1.

Tian, Z., M. Perlin, and W. Choi, 2010: Energy dissipation in two-dimensional unsteady plunging breakers and an eddy viscosity model. *J. Fluid Mech.*, **655**, 217–257, doi:10.1017/S0022112010000832.

Wang, D. W., and H. W. Wijesekera, 2018: Observations of breaking waves and energy dissipation in modulated wave groups. *J. Phys. Oceanogr.*, **48**, 2937–2948, doi:10.1175/JPO-D-17-0224.1.

Wu, C. H., and H. M. Nepf, 2002: Breaking criteria and energy losses for three-dimensional wave breaking. *J. Geophys. Res.*, **107 (C10)**, 3177, doi:10.1029/2001JC001077.

Accepted for publication in *Journal of Physical Oceanography*. DOI 10.1175/JPO-D-19-0138.1.

Zappa, C. J., M. L. Banner, R. P. Morison, and S. E. Brumer, 2016: On the variation of the effective breaking strength in oceanic sea states. *J. Physical Oceanogr.*, **46**, 2049–2061, doi: 10.1175/JPO-D-15-0227.1.

Zappa, C. J., W. R. McGillis, P. A. Raymond, J. B. Edson, E. J. Hintsa, H. J. Zemmelink, J. W. H. Dacey, and D. T. Ho, 2007: Environmental turbulent mixing controls on air-water gas exchange in marine and aquatic systems. *Geophys. Res. Let.*, **34 (10)**, doi:10.1029/2006GL028790, l10601.

Zippel, S. F., J. Thomson, and G. Farquharson, 2018: Turbulence from breaking surface waves at a river mouth. *J. Phys. Oceanogr.*, **48**, 435–453, doi:10.1175/JPO-D-17-0122.1.

Accepted for publication in *Journal of Physical Oceanography*. DOI 10.1175/JPO-D-19-0138.1.

LIST OF TABLES

Accepted for publication in *Journal of Physical Oceanography*. DOI 10.1175/JPO-D-19-0138.1.

Case no.	S_g	f_c (1/s)	T_s (s)	L_s (m)	h/L_s	L_x/L_s	$L_y/2L_s$
T1	0.44	0.7	1.8	5.1	0.59	5	0.8
T2	0.32	0.7	1.8	5.1	0.59	5	0.8
T3	0.40	0.9	1.4	3.0	0.42	4	1.0

TABLE 1. Input parameters for the simulated short-crested (3-D) focused wave packets. In all three cases $N = 10$, $\Delta f/f_c = 0.75$, $T_g/T_s \approx 9.5$, $x_f/L_s \approx 1.6 \sim 1.9$, $y_f = 0$, and $t_f = 15.0$ s. Definitions of all parameters presented here are given in §2.b.

Accepted for publication in *Journal of Physical Oceanography*. DOI 10.1175/JPO-D-19-0138.1.

α_0^b	c_1	c_2	d_1	d_2
1/3	0.67 (±0.21)	4.30 (±0.50)	-0.89 (±0.15)	-3.00 (±0.3)
1	0.48 (±0.12)	3.15 (±0.26)	-0.79 (±0.13)	-2.90 (±0.3)
3	0.26 (±0.12)	2.20 (±0.25)	-0.73 (±0.12)	-2.84 (±0.3)

TABLE 2. The empirical coefficients in Eqs. (15) and (16) for three values of α_0^b (%) obtained using the least squared curve fitting. Coefficients in parentheses represent 95% confidence intervals.

Accepted for publication in *Journal of Physical Oceanography*. DOI 10.1175/JPO-D-19-0138.1.

Table A1. Summary of mathematical variables and symbols used in §3-§5. Here [-] indicates that the corresponding variable is dimensionless. The order of the symbols are consistent with the order of their first appearance in §3-§5.

Symbol	Definition	Units
ε	TKE dissipation rate	[$\mathrm{m^2 s^{-3}}$]
ν_{sgs}	SGS eddy viscosity	[$\mathrm{m^2 s^{-1}}$]
ε_{sgs}	Energy transfer rate from the resolved to SGS motions	[$\mathrm{m^2 s^{-3}}$]
$\breve{\varepsilon}_{sgs}$	Horizontal average of ε_{sgs} in a surface-following reference frame	[$\mathrm{m^2 s^{-3}}$]
$\overline{\varepsilon}_{sgs}$	Time-averaged ε_{sgs} over a few wave periods obtained from one Lagrangian virtual drifter	[$\mathrm{m^2 s^{-3}}$]
$\overline{\overline{\varepsilon}}^L$	Time-averaged ε_{sgs} over many wave periods obtained from all the Lagrangian virtual drifters	[$\mathrm{m^2 s^{-3}}$]
$\overline{\overline{\varepsilon}}^L_n$	Time-averaged ε_{sgs} obtained from n randomly selected Lagrangian virtual drifters	[$\mathrm{m^2 s^{-3}}$]
$\overline{\overline{\varepsilon}}^E$	Time-averaged $\breve{\varepsilon}_{sgs}$ over many wave periods	[$\mathrm{m^2 s^{-3}}$]
f_s	Spectrally-weighted frequency of a wave filed (Eq. 6)	[$\mathrm{s^{-1}}$]
f_p	Peak frequency of a wave filed	[$\mathrm{s^{-1}}$]
T_s	$= 1/f_s$	[s]
T_p	$= 1/f_p$	[s]
T_g	Wave packet period	[s]
L_s	Characteristic wave length calculated based on f_s	[m]
L_p	Characteristic wave length calculated based on f_p	[s]
η	Free surface elevation	[m]
z_{sf}	Vertical elevation in a surface-following reference frame	[m]
H_s	Significant wave height	[m]
H_{eq}	Characteristic wave breaking height (Eq. 7)	[m]
W	Whitecap coverage	[-]
W_A	Active whitecap coverage	[-]
λ	$= W_A/W$	[-]
U_{10}	10-m wind speed	[$\mathrm{ms^{-1}}$]
$\int \overline{\overline{\varepsilon}} dz_{sf}$	$= \int \overline{\overline{\varepsilon}} dz$, total energy dissipation rate	[$\mathrm{m^3 s^{-3}}$]
$\int \overline{\overline{\varepsilon}}_0 dz_{sf}$	Total energy dissipation rate due to background processes	[$\mathrm{m^3 s^{-3}}$]
$\mathscr{L}$	Record length	[s]
α^b	Bubble void fraction	[-]
α^b_0	Bubble void fraction threshold above which the data is assumed to be occluded by bubbles	[-]
$\mathscr{C}$	The correction factor defined in Eq. 13	[-]
$\hat{T}_p$	Clustered averaged T_p within U_{10} bins	[s]
$\hat{U}_{10}$	Clustered averaged U_{10}	[$\mathrm{ms^{-1}}$]
$\hat{u}_*$	Air side friction velocity	[$\mathrm{ms^{-1}}$]
c_p	$= L_p/T_p$	[$\mathrm{ms^{-1}}$]
c	Wave phase speed	[$\mathrm{ms^{-1}}$]
b	Breaking strength parameter	[-]
Ak	Wave steepness	[-]
$\Lambda(c)$	Distribution of the breaking wave crest lengths per unit sea surface area per unit increment in velocity c	[$\mathrm{m^{-2} s}$]
F	Wind energy input rate	[$\mathrm{m^3 s^{-3}}$]

Accepted for publication in *Journal of Physical Oceanography*. DOI 10.1175/JPO-D-19-0138.1.

LIST OF FIGURES

Accepted for publication in *Journal of Physical Oceanography*. DOI 10.1175/JPO-D-19-0138.1.

Accepted for publication in *Journal of Physical Oceanography*. DOI 10.1175/JPO-D-19-0138.1.

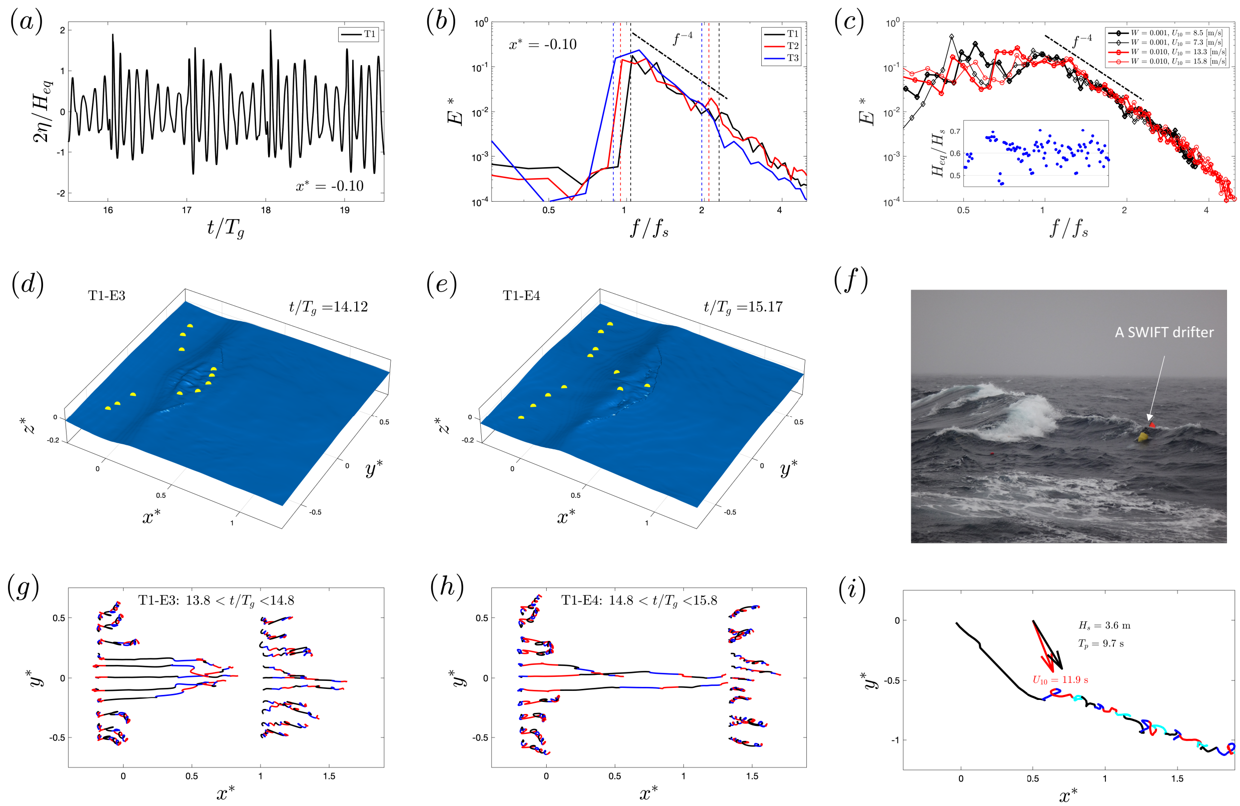

FIG. 1. Comparison between model and field conditions. (a) Temporal variation of the normalized free surface elevations $2\eta/H_{eq}$ for the case T1 and (b) its normalized power spectral density $E^* = E H_{eq}^{-2} f_s$ for all three cases at $(x^*, y^*) = (-0.1, 0)$. (d,e) Snapshots of the spatial variation of the normalized free surface elevations and of the virtual drifters initially released at $x^* = -0.2$ for the breaking events E3 and E4 of the case T1. (g,h) The normalized horizontal displacements of the virtual drifters shown in (d,e). (c,f,i) Examples of E^*, H_{eq}/H_s, a SWIFT drifter, and the horizontal displacement of a SWIFT drifter from the previous field observations in the vicinity of OWS-P at 50° N, 145° W (Thomson et al. 2016). Vertical dashed lines in (b) show f_1/f_s and f_N/f_s respectively. In (i), the horizontal displacement is measured from the initial location of a drifter and is normalized by the wavelength corresponding to $T_p/2$ ($\approx$ 37m here), and arrows show the direction of the surface wind and peak wave component. In (g,h) and (i), each color segment represents the horizontal displacement during T_s and $T_p/2$ respectively.

Accepted for publication in *Journal of Physical Oceanography*. DOI 10.1175/JPO-D-19-0138.1.

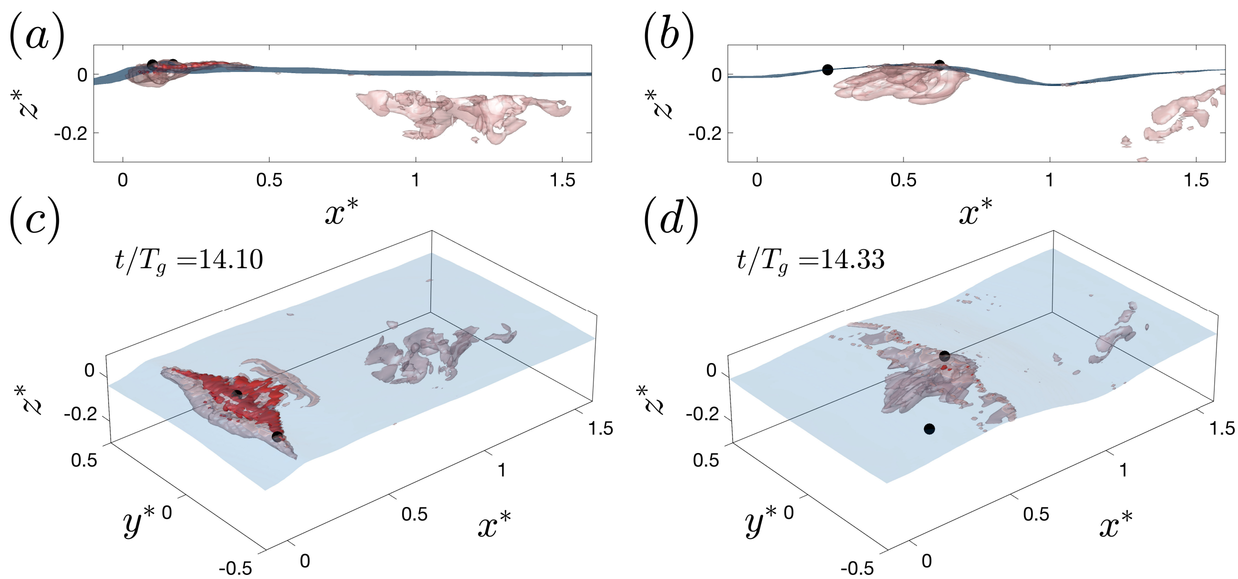

FIG. 2. Side-view (a,b) and 3-D view (c,d) of two snapshots of the spatial variation of the turbulence dissipation rate ε_{sgs} for the breaking event E3 of the case T1. Dark and light iso-surfaces show $\varepsilon_{sgs} = 0.1$ and 10^{-4} ($\mathrm{m}^2\ \mathrm{s}^{-3}$) respectively. Markers show the location of the two virtual drifters that are initially released at $(x^* = 0, y^* = -0.3)$ and $(x^* = 0, y^* = 0)$. The waves propagate in the positive x direction. The patches of sub-surface ε_{sgs} in $x^* > 0.75$ correspond to the preceding breaking event.

Accepted for publication in *Journal of Physical Oceanography*. DOI 10.1175/JPO-D-19-0138.1.

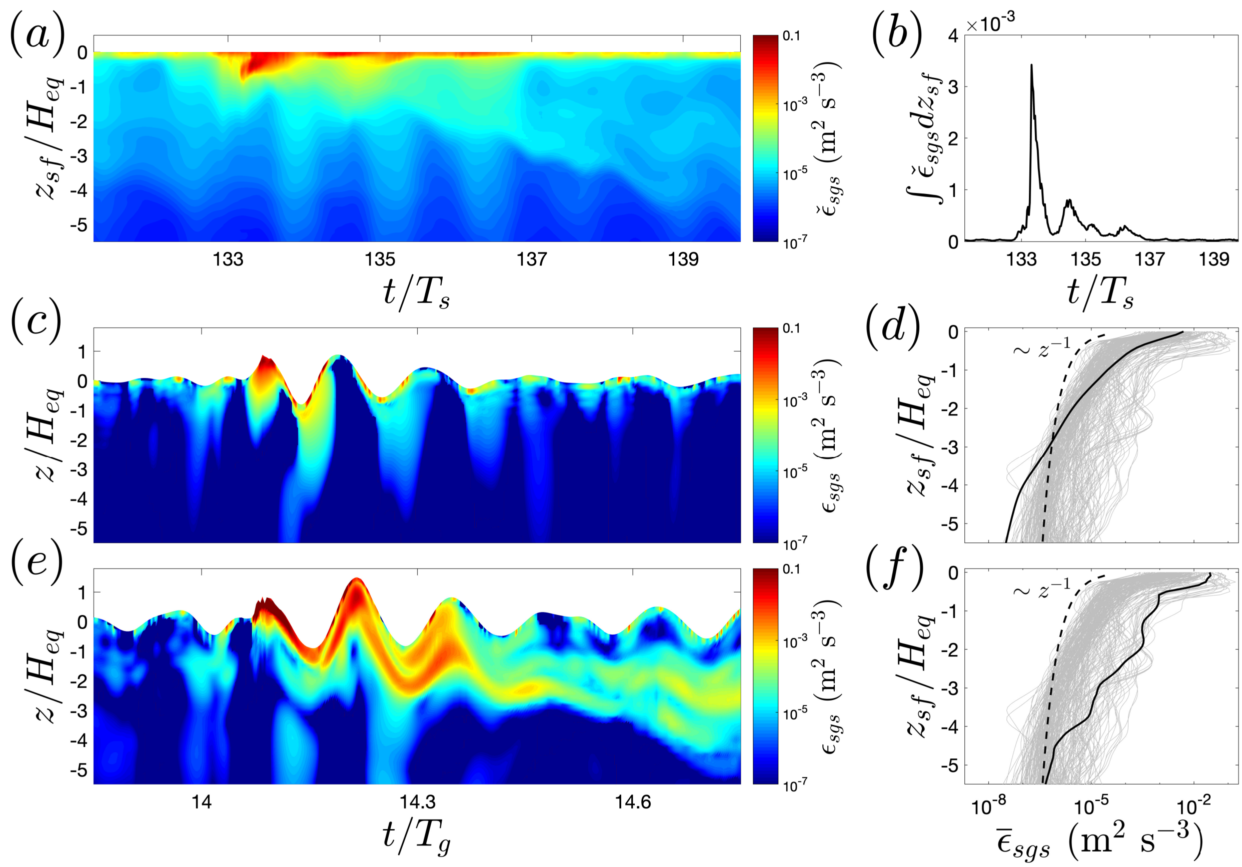

859 FIG. 3. Various measures of the turbulence dissipation rate ε_{sgs} for the breaking event E3 of the case T1. (a) Phase-resolved horizontal-averaged turbulence dissipation rate $\check{\varepsilon}_{sgs}$ in the surface following reference frame, (b) temporal variation of the vertically integrated $\check{\varepsilon}_{sgs}$, (c,e) phase-resolved ε_{sgs} sampled by the two virtual drifters shown in Figure 2, and (d,f) their corresponding time-averaged vertical profiles, $\overline{\varepsilon}_{sgs}$ (thick black lines) as well as the results for all available virtual drifters released at before the beginning of the breaking event T1-E3 (thin gray lines). The dashed lines in panels (d) and (f) demonstrate that $\overline{\varepsilon}_{sgs}$ does not follow the law-of-the-wall vertical scaling ($\sim 1/z$).

Accepted for publication in *Journal of Physical Oceanography*. DOI 10.1175/JPO-D-19-0138.1.

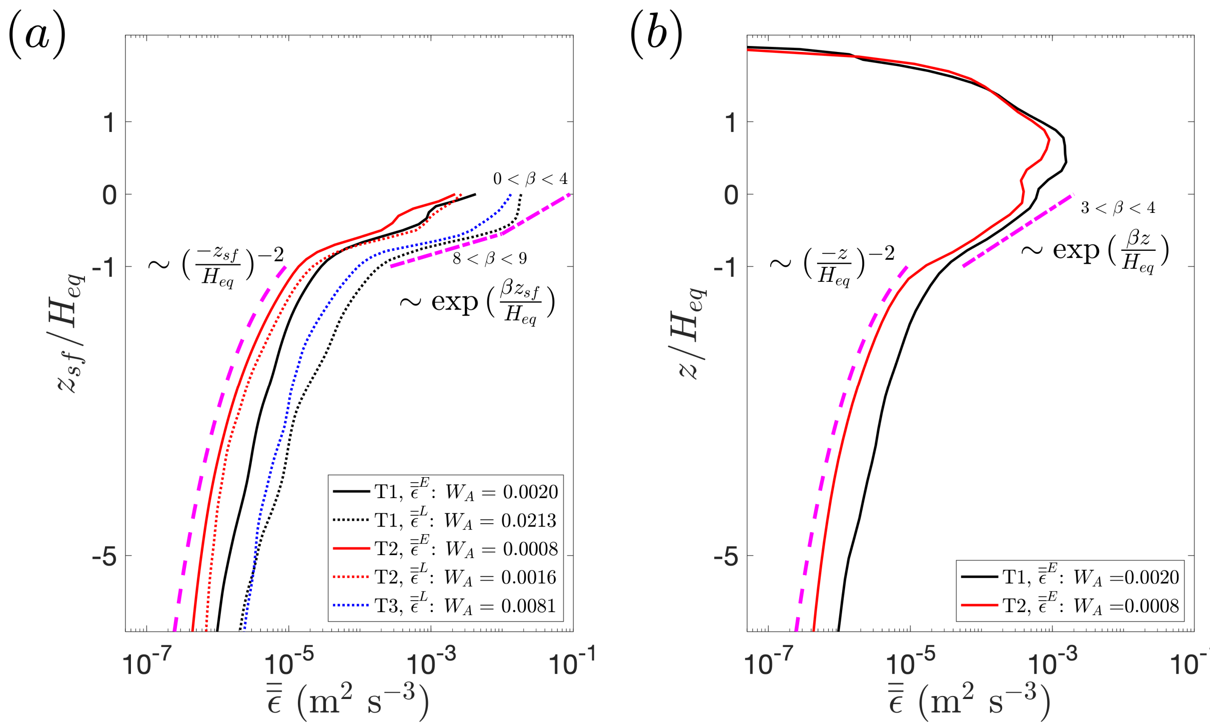

FIG. 4. Model results of the vertical profile of the ensemble-time-averaged turbulence dissipation rates $\overline{\overline{\varepsilon}}$ in (*a*) the surface-following reference frame, and (*b*) the fixed reference frame. Here H_{eq} the equilibrium wave height, W_A the active whitecap coverage, $\overline{\overline{\varepsilon}}^L$, and $\overline{\overline{\varepsilon}}^E$ are defined in Eqs. (7), (9), (10), and (11), respectively.

Accepted for publication in *Journal of Physical Oceanography*. DOI 10.1175/JPO-D-19-0138.1.

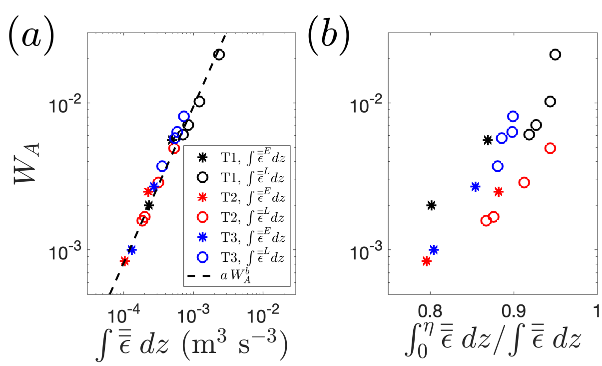

869 FIG. 5. Model results of the variation of (a) the vertically integrated long-time-averaged dissipation rates, and
870 (b) the fraction of total dissipation above still water level $z = 0$ with the active whitecap coverage W_A (Eq. 9).

Accepted for publication in *Journal of Physical Oceanography*. DOI 10.1175/JPO-D-19-0138.1.

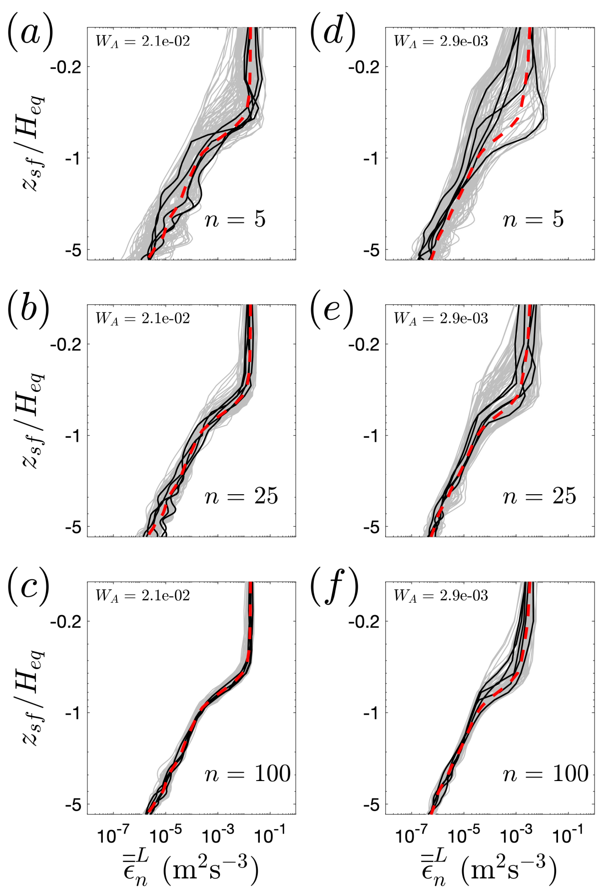

FIG. 6. Variation of the Lagrangian statistics of turbulence dissipation rates obtained from n randomly selected virtual drifters $\overline{\overline{\varepsilon}}_n^L$ (solid lines) with the signal length $\mathscr{L} \approx 9.5nT_s$ for cases with $(a-c)$ $W_A = 2.1 \times 10^{-2}$, and $(d-f)$ $W_A = 2.9 \times 10^{-3}$. For better visibility, five examples of $\overline{\overline{\varepsilon}}_n^L$ profiles are plotted in each frame as individual black curves. The red dashed lines show $\overline{\overline{\varepsilon}}^L$, which represents the average of all virtual drifters (Eq. 10).

Accepted for publication in *Journal of Physical Oceanography*. DOI 10.1175/JPO-D-19-0138.1.

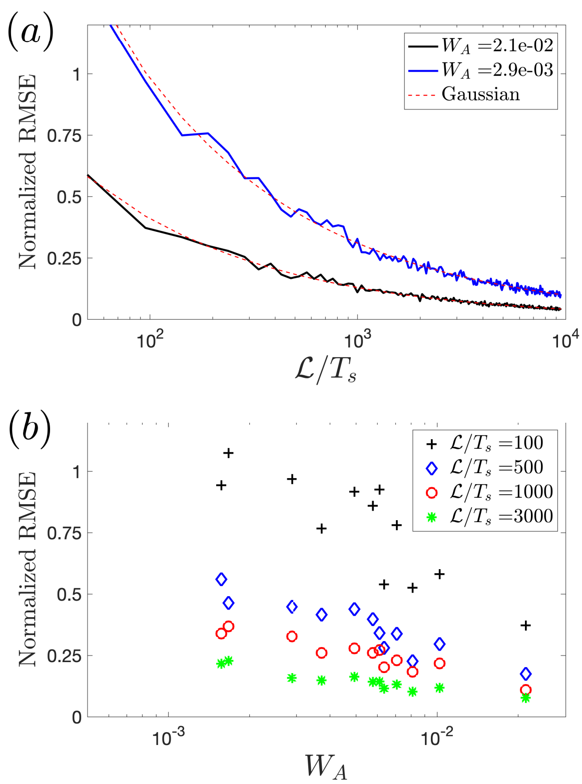

875 FIG. 7. Variation of the normalized standard error of total turbulence dissipation rate estimates (a) with
876 the signal length $\mathscr{L}/T_s \approx 9.5n$, and (b) with active whitecap coverage W_A. The dashed lines in (a) show the
877 normalized standard error estimation using the Gaussian distribution.

Accepted for publication in *Journal of Physical Oceanography*. DOI 10.1175/JPO-D-19-0138.1.

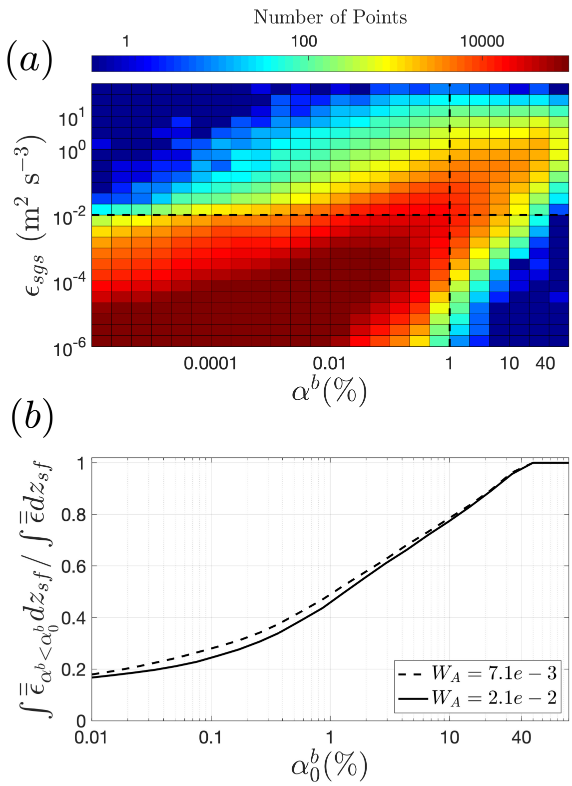

878 FIG. 8. (a) Example of a 2-D histogram of the model results of the local turbulence dissipation rates ε_{sgs} and
879 bubble void fraction, and (b) two examples of the variation of the fraction of the total dissipation within the
880 regions with $\alpha^b < \alpha_0^b$ against α_0^b. In (a), the vertical and horizontal dashed lines show $\alpha^b = 1\%$ and $\varepsilon_{sgs} = 0.01$
881 [m^2 s^{-3}], respectively.

Accepted for publication in *Journal of Physical Oceanography*. DOI 10.1175/JPO-D-19-0138.1.

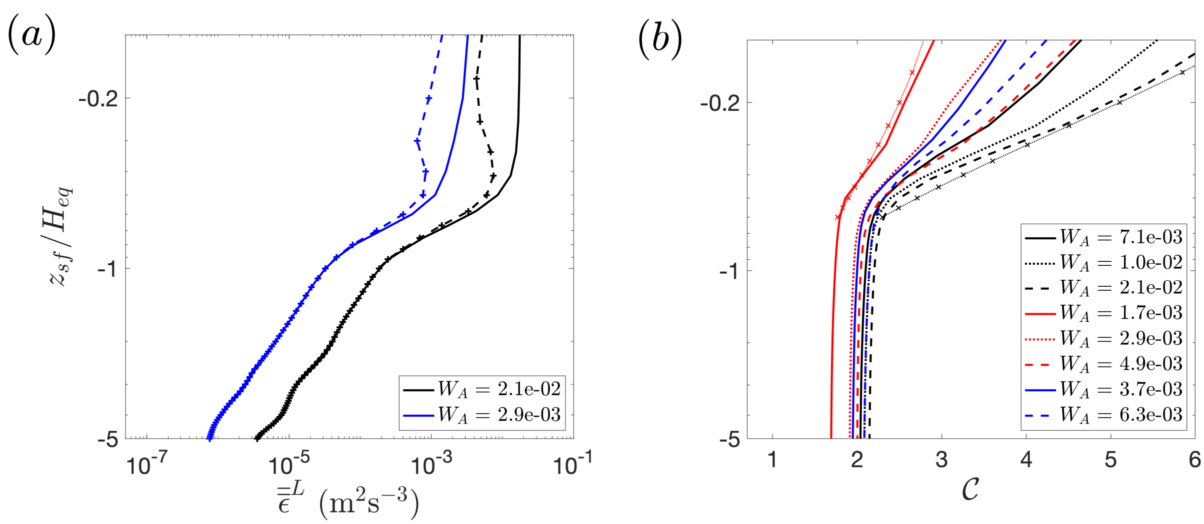

FIG. 9. Incomplete sampling of turbulence dissipation rates. (a) Effect of the bubble occlusion on the Lagrangian averages by considering (solid lines) all model results $\overline{\overline{\varepsilon}}^L$ (Eq. 10), and (dashed lines) only data points in which $\alpha^b < 1\%$. (b) Variation of the correction factor $\mathscr{C}$ (Eq. 13) with depth and the active whitecap coverage W_A. In (b), the two line segments with markers show the fit defined in Eq. 14 for the smallest and largest W_A values of the simulated cases.

Accepted for publication in *Journal of Physical Oceanography*. DOI 10.1175/JPO-D-19-0138.1.

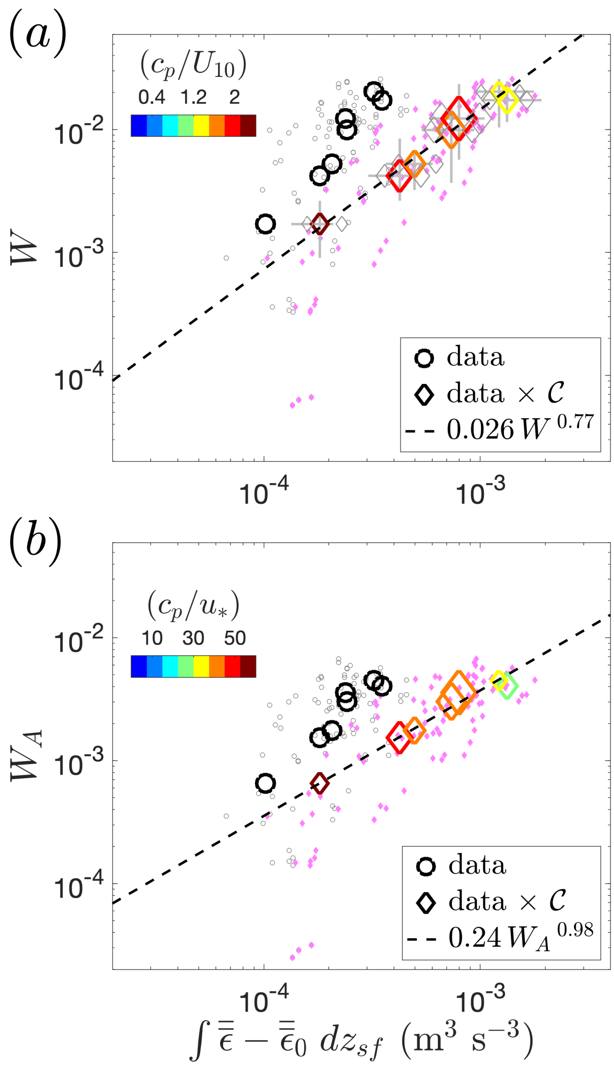

FIG. 10. Variation of the total wave-breaking-induced TKE dissipation rates with (a) total whitecap coverage W, and (b) active whitecap coverage $W_A = \lambda W$ (Eq. 18). Circles show the raw data provided by Schwendeman and Thomson (2015), and diamonds show the corrected results by applying the correction factor $\mathscr{C}$ defined in Eqs. (14-16, $\alpha_0^b = 1\%$). Small and large symbols represent the results considering an averaging time of $\mathscr{L} = 512\mathrm{s} \approx 40 - 80T_p$ and those obtained by a conditional clustered-averaging explained in the text with $\mathscr{L} > 400\hat{T}_p$. The horizontal line segments represent sensitivity of the results with respect to $0.1 < \lambda < 0.75$. The small gray diamonds show the sensitivity of the corrected clustered-averaged total dissipation rates with respect to the variation of the resulting correction factor $\mathscr{C}$ for the choice of $\alpha_0^b = 1/3\%$ and 3%. Vertical line segments represent the range of the observed W values for each bin.

Accepted for publication in *Journal of Physical Oceanography*. DOI 10.1175/JPO-D-19-0138.1.

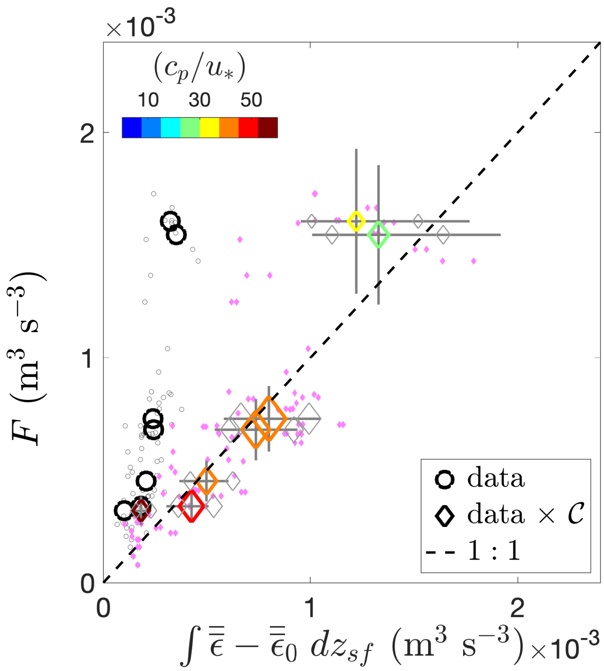

FIG. 11. Variation of the total wave-breaking-induced TKE dissipation rates with the rate of wind energy input F. Vertical line segments represent the sensitivity of F values with respect to $2 < c_e < 3$. Definitions of the rest of symbols and lines are the same as in Figure 10.

Accepted for publication in *Journal of Physical Oceanography*. DOI 10.1175/JPO-D-19-0138.1.